

MULTIPLE PATHS OF DEUTERIUM FRACTIONATION IN PROTOPLANETARY DISKS

Yuri Aikawa

Department of Astronomy, The University of Tokyo

aikawa@astron.s.u-tokyo.ac.jp

Kenji Furuya

Center for Computational Sciences, University of Tsukuba, Japan

Ugo Hincelin

Department of Chemistry, The University of Virginia, USA

and

Eric Herbst

Department of Chemistry, The University of Virginia, USA

ABSTRACT

We investigate deuterium chemistry coupled with the nuclear spin-state chemistry of H_2 and H_3^+ in protoplanetary disks. Multiple paths of deuterium fractionation are found; exchange reactions with D atoms, such as $\text{HCO}^+ + \text{D}$, are effective in addition to those with HD. In a disk model with grain sizes appropriate for dark clouds, the freeze-out of molecules is severe in the outer midplane, while the disk surface is shielded from UV radiation. Gaseous molecules, including DCO^+ , thus become abundant at the disk surface, which tends to make their column density distribution relatively flat. If the dust grains have grown to millimeter size, the freeze-out rate of neutral species is reduced, and the abundances of gaseous molecules, including DCO^+ and N_2D^+ , are enhanced in the cold midplane. Turbulent diffusion transports D atoms and radicals at the disk surface to the midplane, and stable ice species in the midplane to the disk surface. The effects of turbulence on chemistry are thus multifold; while DCO^+ and N_2D^+ abundances increase or decrease depending on the regions, HCN and DCN in the gas and ice are much reduced at the innermost radii, compared with the model

without turbulence. When cosmic rays penetrate the disk, the ortho-to-para ratio (OPR) of H_2 is found to be thermal in the disk, except in the cold ($\lesssim 10$ K) midplane. We also analyze the OPR of H_3^+ and H_2D^+ , as well as the main reactions of H_2D^+ , DCO^+ , and N_2D^+ to analytically derive their abundances in the cold midplane.

Subject headings: astrochemistry — star-formation — protoplanetary disks

1. INTRODUCTION

In the primordial material in the Solar System, such as comets and meteorites, molecular D/H ratios are often higher than the elemental D/H ratio, which is 2×10^{-5} (Geiss & Gloeckler 1998). For example, the D/H ratio of water is found to be $(1.6 - 5) \times 10^{-4}$ in comets (e.g. Mumma & Charnley 2011; Altwegg et al. 2015). Since the zero-point energy of D-bearing species is lower than that of the normal isotope by up to a few hundred K, the significant deuterium enrichment is considered to originate in chemistry at low temperatures.

There are two possible sites of such low-temperature chemistry: molecular clouds prior to star formation and outer regions of protoplanetary disks. In molecular clouds, the temperature is ~ 10 K and high D/H ratios are found for various molecules. For example, even a doubly deuterated molecule, D_2CO , has been detected in prestellar cores, and the $n(\text{D}_2\text{CO})/n(\text{H}_2\text{CO})$ ratio has been derived to be $0.01 - 0.1$ (Bacmann et al. 2003), where $n(i)$ denotes the number density of species i . In such dense cold cores, where HD is the primary reservoir of deuterium, deuterated H_3^+ is produced via exothermic exchange reactions; e.g.,



The high D/H ratio of H_3^+ propagates to other molecules via ion-molecule reactions in the gas phase. The atomic D/H ratio is also enhanced through the electron recombination of H_3^+ and H_2D^+ . The high atomic D/H ratio propagates to icy molecules through hydrogenation/deuteration of atoms and molecules on grain surfaces. The ions H_2D^+ and D_2H^+ are actually detected at the center of the prestellar core L1544 (Caselli et al. 2003; Vastel et al. 2006). In such a dense cold region, the D/H ratio of H_3^+ is further enhanced by the freeze-out of CO, which is otherwise the major reactant of H_3^+ and its isotopologs.

Protoplanetary disks are also partially ionized by X-rays and/or cosmic rays, and the temperature is $\lesssim 20$ K in the outer midplane region, so that deuterium enrichment can proceed in disks, as well. In fact, DCN, DCO^+ , and N_2D^+ have been detected in several disks (e.g. van Dishoeck et al. 2003; Qi et al. 2008; Huang & Öberg 2015). While a

stable neutral species such as DCN can originate in interstellar ice, then delivered to and desorbed in the disk, molecular ions are apparently formed in situ, considering their short destruction timescales. van Dishoeck et al. (2003) used the JCMT telescope to derive a disk-averaged $n(\text{DCO}^+)/n(\text{HCO}^+)$ ratio of 0.035 in TW Hya, providing evidence of ongoing deuterium enrichment in protoplanetary disks. Although the deuterium enrichment in the primordial material in the Solar System can originate in interstellar chemistry, at least partially, it has been debated if and to what extent the molecular D/H ratios are modified in disks (Aikawa & Herbst 1999; Willacy 2007; Cleeves et al. 2014a). Spatially resolved observations of deuterated ions can specify the region of active deuteration in protoplanetary disks.

The emission of DCO^+ is spatially resolved in the disks around TW Hya (Qi et al. 2008) and HD 163296 (Mathews et al. 2013). In both disks, the DCO^+ emission shows a ring structure, which is considered to reflect the production of DCO^+ by the reaction



The exchange reaction (1) to form H_2D^+ is exothermic only by $\lesssim 250$ K, and thus its backward reaction becomes active at $T \gtrsim 30$ K. Mathews et al. (2013) found that DCO^+ emission shows a ring structure of radius $r = 110 - 160$ au, and argued that the outer radius of the DCO^+ ring corresponds to the CO snow line. The ion DCO^+ is expected to be abundant in the region with temperature $T \sim 19 - 21$ K; at higher temperatures ($T \gtrsim 21$ K), CO and ortho- H_2 (see below) would become abundant enough to destroy the precursor molecules, H_3^+ and H_2D^+ , while at $T \lesssim 19$ K, CO abundance would be too low to make DCO^+ abundant (Mathews et al. 2013). The DCN emission in TW Hya disk, on the other hand, is centrally peaked. This molecule is expected to form primarily via the reaction of N atoms with CHD, which is formed by the dissociative recombination of CH_2D^+ . Since the exothermicity of the exchange reaction



is higher than that of reaction (1), DCN can be abundant even at $T \gtrsim 30$ K (Millar, Bennet, & Herbst 1989; Öberg et al. 2012).

Recent observations of deuterated species in disks, however, challenge the above scenario. Qi et al. (2015) observed DCO^+ in HD 163296 with a higher spatial resolution, and found that the inner edge of the DCO^+ ring is at 40 AU, which is much closer to the central star than derived by Mathews et al. (2013). Huang et al. (2017) observed six protoplanetary disks, spatially resolving DCO^+ , H^{13}CO^+ , H^{13}CN , and DCN in most of them. While the DCO^+ emission tends to be spatially more extended than the DCN emission, the relative distributions of DCO^+ and DCN vary among the disks. While the DCN emission is more

compact than the DCO^+ emission in HD 163296, the radial intensity profiles of DCO^+ and DCN are similar in AS 209, for example. Such variations indicate that multiple paths to deuteration occur in the disks.

On the theoretical side, deuterium chemistry in protoplanetary disks has long been investigated (e.g. Aikawa & Herbst 1999; Willacy 2007; Cleeves et al. 2014a). Recent progress in the study of deuterium fractionation includes the evaluation of the state-to-state rate coefficients of the $\text{H}_3^+ + \text{H}_2$ system (Hugo et al. 2009) and the re-evaluation of the exothermicity of reaction (3) (Roueff et al. 2013). Since the ground-state energy of ortho- H_2 (o- H_2) is higher than that of para- H_2 (p- H_2), the backward reactions of exchange reactions such as (1) are less endothermic with o- H_2 than with p- H_2 . The deuterium enrichment would thus be less efficient if o- H_2 is abundant. Although several groups have presented the deuterium chemistry in disks coupled with ortho-para chemistry, they concentrated mostly on molecular species such as HDO rather than DCO^+ and DCN , or made an assumption that the ortho-para chemistry is locally thermalized (Albertsson et al. 2014; Cleeves et al. 2014a, 2016). One of the exceptions is the paper by Teague et al. (2015); these authors observed HCO^+ and DCO^+ lines in DM Tau, and calculated molecular evolution in a disk model to be compared with their observations. While they solved for the spin states of H_2 and H_3^+ , they did not seem to adopt the updated exothermicity for reaction (3). Roueff et al. (2013) calculated the exothermicity of reaction (3) for p- H_2 to be 654 K, which is higher than the previous estimate of 370 K (Smith et al. 1982). Favre et al. (2015) adopted this updated energy difference for reaction (3) in their chemical model, and showed that it enhances the abundance of DCO^+ in the warm surface layers of the disk. Their model, however, does not include the ortho-para chemistry, and implicitly assumes that all H_2 is in the para state. The assumption would not be appropriate in the warm layers.

In the present work, we investigate the deuteration paths of HCO^+ , N_2H^+ , and HCN in protoplanetary disks using an updated chemical reaction network with deuterium fractionation and ortho-para chemistry. Instead of constructing best-fit models of observed disks, we investigate the chemistry in template disk models. The effects of elemental C/O ratio, grain size, vertical mixing, and exclusion of cosmic rays are also studied. The rest of the paper is organized as follows. Our chemical reaction network and protoplanetary disk models are described in §2. Section 3 presents the results of our numerical calculations; i.e., abundance and column density distributions of HCO^+ , N_2H^+ , HCN and their deuterated isotopologs in disk models. The model results are qualitatively compared with observations in §4, and our conclusions are summarized in §5. In appendices, we also present an analysis of the OPRs of H_2 , H_3^+ , and H_2D^+ , and analytical formulae of abundances of H_2D^+ , DCO^+ and N_2D^+ in the cold midplane.

2. MODELS

We adopt basically the same disk structure and chemical reaction network as in Aikawa et al. (2015). Although basic descriptions of the model and network are given in this section, more detailed descriptions can be found in Aikawa et al. (2015), Furuya et al. (2013), and Aikawa & Nomura (2006).

2.1. Disk Models

In the present work, we investigate deuterium chemistry in template disk models, rather than constructing a model for a specific object. The radial distribution of the gas column density in our models is thus rather arbitrary; it is determined so that the mass accretion rate ($10^{-8}M_{\odot}/\text{yr}$) is constant at all radii for a constant viscosity parameter α (see §3.3). Note that we do not explicitly take into account the radial accretion of gas and dust in solving the chemical reaction network. The central star is assumed to be a T Tauri star of mass $M_{*}=0.5 M_{\odot}$, surface temperature $T_{*} = 4000$ K, and radius $R_{*} = 0.5R_{\odot}$. We refer to the UV and X-ray spectrum of TW Hya, and adopt the luminosities of $L_{\text{UV}} = 10^{31}$ erg s $^{-1}$ and $L_{\text{X}} = 10^{30}$ erg s $^{-1}$ (Herczeg et al. 2002; Kastner et al. 2002)(see also Nomura & Millar 2005; Nomura et al. 2007). The vertical density distribution is set by hydrostatic equilibrium. The temperatures of gas and dust are obtained by solving two-dimensional radiative transfer and the balance between cooling and heating. The temperature and density structures are solved self-consistently. The gas and dust temperatures are the same in the midplane, while gas is warmer than dust at the disk surface, which is basically a dense photon-dominated region.

In our fiducial model, the grains have grown to the maximum size a_{max} of 1 mm size, while the minimum size is $a_{\text{min}} = 0.01 \mu\text{m}$, with the dust-to-gass mass ratio of 0.01, all over the disk. A grain size distribution is assumed to follow the power law $dn(a)/da \propto a^{-3.5}$, where $n(a)$ is the number density of grains with size a . For comparison, we also adopt a disk model with dust appropriate to dark clouds, which we label dark cloud dust. The maximum grain size of the latter model is $10 \mu\text{m}$ (Weingartner & Draine 2001). The density and temperature distributions of the two disk models are shown in Figure 1. The temperature is generally higher in the model with dark cloud dust, because it absorbs stellar radiation more efficiently. While we assume that the disk is static (i.e. no diffusion or accretion), we also calculate models with vertical mixing (Furuya et al. 2013), in order to investigate its effect on deuterium chemistry,

2.2. Chemical Model

The gas-grain chemical reaction network is based on Garrod & Herbst (2006), but has been updated to include reactions that are effective at high temperatures ($T \gtrsim 100$ K) (Harada et al. 2010, 2012). Our network includes up to triply deuterated species, and nuclear spin states of H_2 , H_3^+ , and their isotopologs (Hugo et al. 2009; Hincelin et al. 2014; Coutens et al. 2014; Furuya et al. 2015). We refer to Roueff et al. (2013) for the reaction rate coefficients and exothermicities/endothermicities of the exchange reaction (3) and analogous reactions with multi-deuteration and spin states.

Ultra violet radiation from the central star and interstellar radiation field causes photodissociation and photoionization in the gas phase; the rate coefficients are calculated by convolving the dissociation/ionization cross sections of molecules and the UV spectrum at each position in the disk. Self- and mutual shielding of H_2 , HD, CO, N_2 , and C atoms are taken into account (Draine & Bertoldi 1996; Visser et al. 2009; Wolcott-Green & Haiman 2011; Li et al. 2013; Kamp & Bertoldi 2000). The shielding of D_2 is not considered in the present model, but we confirmed that it does not affect our results, because D_2 is much less abundant than HD at the disk surface, where photodissociation is effective. Photodissociation of icy molecules is also considered in our model (e.g. Furuya et al. 2013). The ionization sources in the disk are X-rays, cosmic rays, and the decay of radioactive nuclei. We assume a cosmic-ray ionization rate of $5 \times 10^{-17} \text{ s}^{-1}$ with an attenuation length of 96 g (Umebayashi & Nakano 1981). Considering that the penetration of cosmic rays can be prohibited by stellar winds, we also run a model without cosmic rays (Aikawa et al. 1999; Cleaves et al. 2014b); the disk midplane is then mainly ionized by the decay of radioactive nuclei with a rate of 10^{-18} s^{-1} . Layers above the midplane are mainly ionized by stellar X-rays; the ionization rate could reach 10^{-14} s^{-1} at the disk surface, for example (see Figure 1 in Aikawa et al. 2015).

We adopt a two-phase model, which consists of a gas phase and an undifferentiated grain ice mantle. The sticking probability is assumed to be unity when a neutral atom or molecule collides with a grain surface, except for H and D atoms, for which we adopt the temperature-dependent sticking probability of Tielens & Hollenbach (1985). Adsorption energies of molecules on grain surfaces are generally taken from Garrod & Herbst (2006). The adsorption energies of deuterated species are generally set to be the same as those of normal species. One exception is the D atom, the adsorption energy of which is set to be 21 K higher than that of the H atom, which is assumed to be 600 K (Caselli et al. 2002). The adsorption energies of CO, N_2 and HCN, the abundance of which we present in the following section, are set to be 1150 K, 1000 K, and 3370 K, respectively. The value for HCN is adopted from the Temperature Programmed Desorption (TPD) experiment by Noble et al.

(2013). The dependence of molecular abundances on the adsorption energies of CO and N₂ are presented in Aikawa et al. (2015).

In addition to thermal desorption, we take into account three non-thermal desorption processes: photodesorption, stochastic heating by cosmic rays, and reactive desorption (e.g. Öberg et al. 2009a; Hasegawa & Herbst 1993; Garrod et al. 2007). The efficiency of chemical desorption is set to be $10^{-4} - 10^{-2}$ depending of the reactions, referring to Garrod et al. (2007). Recent laboratory experiments show that the efficiency depends on the molecular composition of the grain surface (Minissale et al. 2016). In order to include such an effect, we need to adopt the three-phase model, discriminating the ice surface from the bulk ice mantle, which we postpone to future work. We assume that the surface reactions occur via the Langmuir-Hinshelwood mechanism; i.e. the adsorbed species diffuse on grain surfaces via thermal hopping, and react with each other when they meet, before they desorb. The modified rate of Caselli et al. (1998) is adopted to ensure that the rate of hydrogenation (deuteration) is not higher than the adsorption rate of H atoms (D atoms) when the number of such atoms on a grain is small ($\lesssim 1$). The barrier for thermal hopping (E_{diff}) is set to one-half of the adsorption energy (E_{ads}). Lower values from 0.3 to 0.4 have also been used in astrochemical models (e.g. Ruaud et al. 2016; Penteado et al. 2017); the surface reactions become more rapid with the lower ratio of $E_{\text{diff}}/E_{\text{ads}}$. The efficiency of H₂ formation and those of its isotopologs on granular surfaces become lower in warmer regions (e.g. $T \gtrsim$ a few 10 K) in the disk, since the physisorbed H (and D) atoms are desorbed more promptly. When the temperature is high enough, however, a bare grain surface appears, on which H atoms can be chemisorbed. At such high temperatures, we assume that the formation rate of H₂ is 0.2 times the sticking rate of H atom onto grain surfaces, referring to Cazaux & Tielens (2004, 2010) (see eq. 19 of Furuya et al. 2013).

The elemental abundance of deuterium is set to be 1.5×10^{-5} relative to hydrogen (Linsky 2003). The initial molecular abundances are determined by considering the molecular evolution from a cloud formation stage to a collapse phase to form a protostar. Furuya et al. (2015) first calculated molecular evolution behind the shock front of colliding HI gas. Furuya et al. (2016) then calculated the subsequent molecular evolution in the hydrostatic prestellar core and in its collapse phase to form a protostar, as in Aikawa et al. (2012). We adopt the fiducial model of Furuya et al. (2016) for our initial abundances; the shock model is run until the column density of the post shock gas reaches a visual extinction of 2 mag, and the duration of the hydrostatic prestellar phase is set to be 10^6 yr. Then the core collapses to form a protostar in 2.5×10^5 yr, and the molecular evolution in the infalling envelope is calculated until the protostar is 9.3×10^4 years old. While Furuya et al. (2016) calculated a spatial distribution of molecular abundances in a protostellar core, our initial abundances for the present work are adopted from the infalling fluid parcel which reaches a radius of 60

au in the core. The initial abundances of major species are presented in Table 1; since the temperature (~ 144 K) and density ($\sim 5 \times 10^7 \text{ cm}^{-3}$) are high in the infalling fluid parcel at 60 au, ices and ions are not abundant. While the OPR of H_2 is initially 3.2×10^{-3} , it reaches thermal equilibrium or steady state in a relatively short timescale (see Appendix A). Our results thus do not significantly depend on the initial OPR of H_2 .

3. RESULTS

In the following, we consider the spatial distributions of HCO^+ , DCO^+ , N_2H^+ , N_2D^+ , HCN , and DCN , and describe the major formation pathways of the deuterated species. We present the results at 3×10^5 yr, which is earlier than a typical age of T Tauri stars (~ 1 Myr), because we do not include radial accretion and/or mixing in the present model. The abundances of HCO^+ and N_2H^+ (and their isotopologs) are strongly coupled with CO and N_2 , which are gradually converted to less volatile species such as CO_2 and NH_3 , and depleted from the gas phase. The timescale of this conversion in the gas phase is, however, $\sim 5 \times 10^5 \left(\frac{\zeta_{\text{He}}}{2.5 \times 10^{-17} \text{ s}^{-1}} \right)^{-1}$ yr, where ζ_{He} is the ionization rate of He atom. It is comparable to or longer than the accretion timescale of the disk at $r \lesssim 100$ au (Furuya & Aikawa 2014)(see also Furuya et al. 2013). In other words, gaseous CO and N_2 can be supplied from the outer radius by viscous accretion and the radial drift of dust grains with ice mantles. The abundances of CO and N_2 are thus underestimated, if we choose 1 Myr in our static models. The temporal variation of the abundance of each molecular species is also described in the following.

3.1. Fiducial Model

3.1.1. HCO^+ and DCO^+

Let us first consider HCO^+ and DCO^+ . The former is mainly formed by the reaction $\text{CO} + \text{H}_3^+$. As a reference, distributions of gaseous CO abundance and its column density are shown in Figure 2 (a) (b), while those of HCO^+ and DCO^+ are shown in Figure 2, panels (c)(d) and (f). The horizontal axis depicts the radius (r) of the disk. In panels (a) (c) (d) and (e), the vertical axis is the distance from the midplane z , normalized by the radius; i.e. z/r , while the vertical axis is the column density for panels (b) and (f). In the panels showing the abundance distributions (a, c and d), the dotted lines depict the positions where the X-ray ionization rate is equal to the cosmic-ray ionization rate ($5 \times 10^{-17} \text{ s}^{-1}$) (the upper dotted line) and to the ionization rate by decay of radio active nuclei ($1 \times 10^{-18} \text{ s}^{-1}$) (the

lower dotted line). The long dashed line indicates the CO snow surface; it indicates the positions where CO abundances in the gas phase and in the ice mantle should be equal, if the abundances are determined simply by adsorption onto grains and thermal desorption. In the layer below the long dashed line, CO is expected to be mainly in the ice mantle, while it is expected to be abundant in the gas phase, elsewhere. The snow line is defined as the radius at which the snow surface crosses the disk midplane.

In our model, CO is gradually converted to less volatile molecules such as CO₂ ice and CH₃OH ice and thus depleted even in the regions inside the CO snow line (~ 20 au) and in the layer above the CO snow surface (Furuya & Aikawa 2014). Although we present the results at 3×10^5 yr, which is shorter than the timescale of chemical conversion in the gas phase, chemical conversion on grain surfaces is more efficient than in the gas phase. In the midplane at $40 \text{ au} \lesssim r \lesssim 100 \text{ au}$, CO (both in the gas phase and in ice mantle), and thus HCO⁺, are deficient ($n(i)/n(\text{H}) \lesssim 10^{-11}$), and such regions with low CO and HCO⁺ abundances extend inwards over time. For example, the gaseous CO abundance is as low as 5×10^{-9} and the HCO⁺ abundance is 1×10^{-12} in the midplane at $r = 10$ au at $t = 1$ Myr. It should be noted that ALMA observations recently revealed such depletion of gaseous CO inside the CO snow line in TW Hya (Nomura et al. 2016; Schwarz et al. 2016) (see also Zhang et al. 2017). In the midplane at inner radii ($r \lesssim 10$ au), the HCO⁺ abundance is limited by the low ionization degree, which occurs at high density. At $r \lesssim 70$ au, molecular ions such as H₃⁺ and HCO⁺ are deficient at $z/r \sim 0.15$, because photoionization makes atomic ions (e.g. S⁺) the dominant positive charge carrier in such upper layers. The high electron abundance then reacts quickly with molecular ions.

Figure 2 (e) depicts the major formation pathways of DCO⁺ at each position in the disk. Comparing panels (d) and (e), we can see that DCO⁺ is abundant in the layer below the CO snow surface (i.e. at the lower z) due to reaction (2), despite the relatively low CO abundance in the gas phase. In the midplane, deuterated-H₃⁺ increases towards the outer radius, where the temperature is lower and the chemical conversion of HD is less efficient (see Appendix B). The chemical conversion of CO is also less efficient at outer radii ($\gtrsim 200$ au). The DCO⁺ abundance thus increases outwards at $r \gtrsim 100$ AU. In the upper layers ($z/r \gtrsim 0.2$), on the other hand, DCO⁺ is mainly formed via



Since the reaction is exothermic by 796 K (Adams & Smith 1985), the backward reaction is less efficient than the forward reaction even at warm temperatures.

These results are basically the same as described in Öberg et al. (2015). One update is that, following Roueff et al. (2013) we set the exothermicities of reaction (3) and its multi-deuterated counterparts to values higher than those previously determined (Smith et al.

1982) and used in Öberg et al. (2015). For example, the exothermicity of $\text{CH}_3^+ + \text{p-H}_2$ and $\text{CH}_3^+ + \text{o-H}_2$ are set to 660 K and 489 K, respectively. Although we do not distinguish the nuclear spin state of CH_3^+ , this omission does not affect our results, since the difference in exothermicities among the reactions with ortho- and para- CH_3^+ is only 6 K (Roueff et al. 2013). Although DCO^+ is also formed via the reaction between CO and CH_4D^+ , where the ion is produced via reaction (3) and subsequent radiative association with H_2 , this path is the major formation path of DCO^+ only in limited regions, i.e. the green regions in panel (e). It is in contrast to the model of Favre et al. (2015), in which reaction (3) significantly contributes to the DCO^+ formation in warm surface layers and thus enhances the DCO^+ column density. Although the direct comparison between our model results and those of Favre et al. (2015) is not straightforward due to the differences in disk physical structure, knowledge of the spin state of H_2 would be a key to differentiate between the two results. While Favre et al. (2015) assumed all H_2 in the para form, and used a constant exothermicity of 654 K for reaction (3), we found that the OPR of H_2 is almost thermal at each position in the disk (see Appendix A); the effective exothermicity of reaction (3) thus decreases as o- H_2 increases with temperature. Figure 3 shows the ratio of the backward to forward reaction rate coefficients referring to Roueff et al. (2013). For the solid line, we assumed that the OPR of H_2 is thermal. The dashed line, on the other hand, shows the ratio when all H_2 is in para state, so that the exothermicity of the forward reaction is constant at 654 K. The dotted line depicts the ratio of the former (i.e. the ratio shown with the solid line) to the latter (the dashed line); it reaches a maximum at the temperature of ~ 30 K, which seems to correspond to the layer with abundant DCO^+ claimed by Favre et al. (2015). It should be noted, however, that the contributions of reaction (3) become more significant when the elemental C/O ratio is higher than unity (§3.2).

Figure 2 (f) shows the radial distributions of column densities of HCO^+ (dashed lines) and DCO^+ (solid lines). The blue, green, and red lines depict the values at $t = 1 \times 10^5$ yr, 3×10^5 yr (the fiducial value), and 9.3×10^5 yr, respectively. Both HCO^+ and DCO^+ increase inwards from $r \sim 40$ au, which is slightly outside the CO snow line (~ 20 AU). In the midplane inside $r \sim 40$ au, thermal desorption of CO becomes non-negligible, which makes HCO^+ the dominant charge carrier, while H_3^+ and its isotopologues dominate in the outer radius (see eq. (23) in Aikawa et al. 2015). Inside a radius of ~ 4 au, the DCO^+ abundance is low in the midplane; the warm temperature lowers the atomic D/H ratio, and the D atom abundance is also lowered by reaction with HS. Outside 50 au, the column density of DCO^+ increases outwards due to its enhancement in the outer midplane, while the HCO^+ column density is relatively flat. Both column densities gradually decrease with time, as CO is converted to less volatile species. The decline of the DCO^+ column density is more significant than that of HCO^+ , since DCO^+ has its abundance peak in the midplane

at outer radii, where CO conversion is efficient.

3.1.2. N_2H^+ and N_2D^+

Figure 4 shows distributions of molecular abundances, column densities, and major formation pathways of deuterium isotopologs as in Figure 2, but for N_2 , N_2H^+ , and N_2D^+ . N_2H^+ is formed by $N_2 + H_3^+$, and is destroyed by recombination with electrons and proton transfer to CO. Thus its abundance depends on N_2 , CO, H_3^+ and electrons (Aikawa et al. 2015); the abundance has a peak around the CO snow surface, where the abundance ratio of CO to electron is $\sim 10^3$, and in the layer above the CO snow surface, where gaseous CO is converted to less volatile species to be frozen onto grains.

In the midplane, N_2 is gradually converted to less volatile species such as NH_3 ice, and thus the region of low N_2H^+ abundance basically expands with time, although N_2H^+ becomes abundant at $t = 9.3 \times 10^5$ yr around the radius of several au, where gaseous CO is reduced by the conversion effect. The formation pathways of N_2D^+ are similar to those of DCO^+ ; N_2D^+ in the midplane is formed by the reaction of N_2 with deuterated H_3^+ , while N_2D^+ is formed by



above the CO snow surface. In the upper layers, the ratio of N_2D^+/N_2H^+ is lower than that of DCO^+/HCO^+ , because the exothermicity of reaction (5) (550 K) is lower than that of reaction (4). The column densities of both N_2H^+ and N_2D^+ have a peak at 20 au $\lesssim r \lesssim$ 50 au. The inner boundary corresponds to the snow line of CO, the main reactant with N_2H^+ , while the outer boundary is slightly outside the N_2 snow line, for a similar reason used for HCO^+ . Outside $r \sim 150$ au, the N_2D^+ column density increases outwards, since it is abundant in the outer midplane.

3.1.3. HCN and DCN

Figure 5 shows the distributions of HCN and DCN, the formation pathways of DCN, and the column densities of HCN and DCN. Since the desorption energy of HCN is high (3370 K), the abundance of gaseous HCN is $\lesssim 10^{-10}$ outside a radius of a few au, where the temperature is $\lesssim 100$ K. HCN in the ice mantle, on the other hand, is as abundant as $10^{-7} - 10^{-6}$ in the midplane. Towards the outer ($r \gtrsim 30$ au) midplane, HCN forms by the dissociative recombination of H_2CN^+ , which forms by $H_3^+ + CN \rightarrow HCN^+ + H_2$ followed by $HCN^+ + H_2 \rightarrow H_2CN^+ + H$. In the upper layers and inner radii, it forms by $H + H_2CN$

and $\text{N} + \text{HCO}$. The precursor molecules H_2CN and HCO are produced by $\text{CH}_3 + \text{N}$ and $\text{CH}_2 + \text{O}$, respectively. HCN also is produced by reactive desorption after the grain surface reaction of $\text{H} + \text{CN}$.

The major formation paths of DCN are mostly the deuterated version of the above reactions. One exception is



which is effective at the disk surface, depicted by the green region in Figure 5 (c). In our model, the activation barrier of both the forward and backward reaction of (6) is set to be 500 K, following Schilke et al. (1992). A more recent quantum chemical calculation (Kayanuma in private communication) evaluates this barrier to be 3271 K, but also predicts that the effect of the barrier would be significantly lowered by tunneling. Our result does not change, even if we assume a higher barrier, e.g. 1800 K, for reaction (6). Another exception is $\text{C}_3\text{H}_4\text{D}^+ + \text{N}$, which dominates in the midplane at $r \sim 6$ au, i.e. the blue region. In this warm midplane region ($40 \text{ K} < T < 50 \text{ K}$), hydrocarbons are also deuterated via



which is exothermic by 550 K. The major exothermic exchange reaction that initiates the enhancement of the DCN/HCN ratio is thus reaction (1) in the outer midplane, while reactions (3) and (7) dominate in the upper layers and in inner radii. It should be noted that HCND^+ and DCNH^+ are not distinguished in our reaction network, which means that the network of DCN and DNC is partially mixed in regions where the recombination of HDCN^+ is their major formation path.

Due to the contribution from the outer midplane, the column density of DCN increases outwards at $r \gtrsim 20$ au. Inside a radius of a few au, both the HCN and DCN column densities are high, since they are relatively abundant in the $z/r \sim 0.06$ and $z/r \sim 0$ layers. In the upper layer, large hydrocarbons in ice mantles such as $\text{H}_5\text{C}_3\text{N}$ serve as reservoirs of carbon and nitrogen, while the reactants of C-bearing species, such as O atoms, are deficient in the midplane with high density.

3.2. Elemental Abundances

Observations in recent years suggest that the surface and molecular layers are deficient in elemental carbon and oxygen, especially in relatively cold disks. Hogerheijde et al. (2011) detected ground-state rotational emission lines of H_2O in the disk around TW Hya using the Herschel Space Observatory to find that the emissions are significantly weaker than expected from disk models. Du et al. (2017) obtained and analyzed the water emission of

13 protoplanetary disks. They compared the observational data with disk models to show that the abundance of gas-phase oxygen needs to be reduced by a factor of at least ~ 100 to be consistent with the observational upper limits and positive detections, if a dust-to-gas mass ratio is 0.01. Meijerink et al. (2009) compared the radiative transfer models with mid-infrared spectrum of H_2O taken by *Spitzer* to find that water vapor is significantly depleted in the disk surface beyond the radius of ~ 1 au. They proposed that water vapor is depleted by the vertical cold finger effect; turbulent diffusion transports the water vapor from the disk surface to the layer below the snow surface, where water can freeze out and transported to the midplane via dust settling. Favre et al. (2013) found that the gaseous CO abundance is low ($10^{-6} - 10^{-5}$) even in the warm molecular layer (above the CO snow surface) in the disk of TW Hya by comparing C^{18}O ($J = 2 - 1$) and HD ($J = 1 - 0$) emission line intensities. Kama et al. (2016) combined various emission lines including CI and OI towards TW Hya and HD100546; carbon and oxygen were found to be strongly depleted from the gas phase in the disk of TW Hya, while the depletion is moderate in the disk of HD100546. Kama et al. (2016) also presented an analytical model of the vertical cold finger effect to show that a combination of turbulent mixing and settling of large dust grains deplete C- and O-bearing volatiles from the surface and molecular layers of disks by locking them in the ices in the midplane (see also Krijt et al. 2016; Xu et al. 2017). Since H_2O is less volatile than CO, such a depletion mechanism would be more efficient for oxygen than carbon, which could enhance the C/O ratio in the surface and molecular layers. Kama et al. (2016) found the C/O ratio to be higher than unity in the disk of TW Hya. Bergin et al. (2016) observed C_2H emission, which is bright in a ring region, in TW Hya and DM Tau. In order to reproduce the bright C_2H emission in disk models, a high C/O ratio (> 1) is required together with a strong UV field.

In order to investigate the depletion of elemental carbon and oxygen on deuterium chemistry, we performed a calculation of our fiducial disk model as in §3.1, but with a modified set of initial abundances. We set the initial abundance of H_2O to zero and reduce the CO abundance by an order of magnitude, while the abundances of other species are the same as in our fiducial model. Even with this reduced abundance, CO is still the major carbon carrier, although CH_4 is the most abundant among C-bearing species (see Table 1). Major oxygen carrier in the initial condition is CO, H_2CO , and CO_2 . The elemental C/O ratio is 1.43. Figure 6 shows the distributions of CO, HCO^+ and DCO^+ abundances (panels a, c, and d), their column densities (panels b and f) and major formation pathways of DCO^+ (panel e). While the spatial distributions of the molecular abundances and column densities of HCO^+ and DCO^+ are basically similar to the fiducial model (Figure 2), there are several notable differences. Firstly, CO depletion via chemical conversion to CO_2 ice is less effective above the CO snow surface in the outer radius ($r \gtrsim 20$ au) than in the fiducial model, which

is natural considering the reduced oxygen abundance. HCO^+ and DCO^+ thus becomes more abundant in the layer above the CO snow surface, in which DCO^+ is mainly formed by reaction (3). The high C/O ratio enhances the abundance of hydrocarbons and thus the importance of reaction (3). In spite of the reduced CO abundance, the column densities of HCO^+ and DCO^+ are similar to those in the fiducial model, except that the depression of the DCO^+ column density at $r \sim 50$ au is more modest and the HCO^+ column density is reduced at the central region ($r \lesssim$ a few au), in which HCO^+ exists mostly in the surface layer.

Figure 7 (a-f) shows the distributions of N_2 , N_2H^+ , and N_2D^+ , their column densities, and the major formation pathways of N_2D^+ . The distributions of N_2 and N_2D^+ are similar to those in our fiducial model (Figure 4), while N_2H^+ is reduced in the layer above the CO snow surface, in which the gaseous CO abundance exceeds that in the fiducial model.

Figure 7 (g-j) shows the distributions of HCN and DCN, their column densities, and the major formation pathways of DCN. Their abundances and column densities are significantly higher than in the fiducial model, since the high C/O ratio enhances the abundance of hydrocarbons, which react with N atoms to form HCN.

We also calculated a model in which the initial abundance of H_2O is totally depleted but CO is not (the C/O ratio then becomes 1.10); the results are quite similar to the model described above, except that CO is more abundant inside the CO snow line, which lowers the N_2H^+ abundance .

3.3. Dust Grain Sizes

Figure 8 shows distributions of gaseous CO, HCO^+ , and DCO^+ (panels a, c and d), the main formation paths of DCO^+ (panel e), and their column densities (panels b and f) in the model with dark cloud dust. The initial abundances are the same as in our fiducial model. Since the total surface area of grains is larger than in the fiducial model, the freeze-out of CO and subsequent conversion to other molecules is more efficient in the dark cloud dust model than in the mm-sized grain model, especially in the midplane regions. In the layer above the midplane, on the other hand, UV radiation is more efficiently attenuated, so that the molecular layer extends to larger z than in Figure 2.

At early time (e.g. $t = 1 \times 10^5$ yr), HCO^+ is abundant in the layer above the CO snow surface, and in the midplane inside the CO snow line. Since the contribution from the upper layers is significant, the radial distribution of the HCO^+ column density is rather flat; although it slightly increases inwards around the CO snow line ($r \sim 100$ au), the increment

is not significant compared with that in Figure 2 at $r \sim 40$ au. HCO^+ in the midplane decreases with time, as CO is converted to less volatile species. Its column density, however, varies by less than a factor of three, due to its constantly high abundance in the upper ($z/r \gtrsim 0.3$) layers.

The DCO^+ ion is mainly formed by reaction (4), since CO is depleted in the midplane, where reaction (2) should be efficient. At the early time, D atoms are abundant in the upper ($z/r \gtrsim 0.2$) warm layers, where reformation of HD is inefficient. DCO^+ at that stage is thus abundant in the upper layers, and its column density distribution is relatively flat at $r \gtrsim 30$ au, including the radius around the CO snow line. Then DCO^+ decreases as D atoms are incorporated into hydrocarbons, and CO inside the snow line is converted to less volatiles species. Its column density thus decreases significantly with time. Even at 9.3×10^5 yr, DCO^+ in the midplane does not significantly contribute to its column density except around a radius of a few tens of au, where the column density has a sharp peak. This is in contrast to the model with mm dust grains, in which DCO^+ in the midplane mostly determines its column density distribution.

In order to check the significance of the updated exothermicity of reaction (3), we also ran a model in which its exothermicity is set to 370 K. Compared with the model with this old value, the DCO^+ abundance is enhanced at $0.3 \lesssim z/r \lesssim 0.4$ at a radius of several tens of au in the present model, although reaction (4) is the dominant formation path for DCO^+ there.

Figure 9 shows the distributions of N_2 , N_2H^+ , HCN and their deuterated isotopologs, their column densities, and the major formation pathways of the deuterated isotopologs in the model with dark cloud dust. N_2H^+ is abundant in the upper layers, where H_3^+ is the dominant ion, and in the midplane region between the snow lines of CO (~ 120 au) and N_2 (~ 230 au). Its abundance in the midplane, however, decreases as N_2 is converted to NH_3 ice in a few $\times 10^5$ yr (Furuya & Aikawa 2014). The distribution of N_2D^+ is similar to that of N_2H^+ , but its abundance in the upper ($z/r \gtrsim 0.3$) layer is lower than the maximum abundance in the midplane. The column density of N_2D^+ , therefore, decreases significantly as N_2 is converted to NH_3 ice in the midplane. The major deuteration path is via H_2D^+ in the midplane, and via D atoms (reaction 5) in the upper layers.

Outside a radius of $r \sim 10$ au, gaseous HCN and DCN are distributed mostly in the upper ($z/r \gtrsim 0.2$) layers, where they form via the recombination of H_2CN^+ (HDCN^+) and reaction H_2CN (HDCN) + H. The radial distributions of their column densities gradually increase outwards at $r \gtrsim 10$ au. At the innermost radii ($r \lesssim 3$ AU), on the other hand, the temperature is high enough ($\gtrsim 100$ K) to desorb HCN and DCN from ice mantles.

We also calculated molecular abundances in the disk model with the maximum grain (pebble) size of 10 cm, and found that the distributions of gaseous molecular abundances are qualitatively similar to those in our fiducial model (i.e. the model with mm-sized dust). Some notable differences are as follows. Firstly, the midplane temperature is slightly higher in the model with cm dust. Secondly, CO is converted to CO₂ ice more efficiently in the model with cm dust inside the CO snow line (around a radius of a few tens of au), because the OH radical, which reacts with CO to produce CO₂, is produced from H₂O ice due to the higher UV flux. Thirdly, gaseous HCN and DCN are more abundant in the model with cm dust outside a radius of a few au; a deeper penetration of UV and slightly warmer temperature enhance their precursors, N atoms and hydrocarbons, in the gas phase. Inside their snow line ($\lesssim 2$ au), on the other hand, HCN and DCN are less abundant in the model with cm dust, since more refractory carbon chains accumulate in the ice mantle.

3.4. Turbulent Mixing

Protoplanetary disks are considered to be turbulent, most probably due to magneto-rotational instability (Balbus & Hawley 1991). The direct measurement of non-thermal velocity dispersion v has been one of the major challenges in radio observations of disks. The dispersion is basically subsonic with a Mach number $\mathcal{M} = v/c_s \sim 0.2 - 0.4$ (Teague et al. 2016), where c_s is the sound speed. While a very low velocity dispersion $\mathcal{M} < 0.03$ is derived in HD163296 (Flaherty et al. 2015), Teague et al. (2016) took into account the uncertainties in flux calibration to derive an upper limit of $\mathcal{M} \sim 0.16$. Since the disk has vertical temperature gradients, and since the mixing timescale in the vertical direction is shorter than that in the radial direction (e.g. Aikawa et al. 1996), the vertical mixing could alter the molecular D/H ratios (Furuya et al. 2013; Albertsson et al. 2014). In this subsection, we investigate the effect of vertical turbulent mixing on chemistry including the D/H ratios.

The diffusion coefficient is of the same order as the kinematic viscosity coefficient, $\alpha c_s H$, where H is the scale height of the disk. Although there could be a slight difference between the two values (e.g. Johansen & Klahr 2001), we assume that the values of the two coefficients are the same in the present work. The non dimensional parameter α is equal to $(v/c_s)(l/H) \approx (v/c_s)^2$, where l is the size of the turbulent eddy. The value of α is thus estimated to be $\lesssim 10^{-2}$ in protoplanetary disks. Figure 10 and Figure 11 show distributions of neutral and ionic species, respectively, in models with a diffusion coefficient $\alpha = 10^{-3}$ (top row) and 10^{-2} (middle row). The bottom panels show the molecular column densities for the model without diffusion (solid lines) and with a diffusion coefficient of $\alpha = 10^{-3}$ (dashed)

and 10^{-2} (dotted). CO and N_2 are also shown in Figure 10 in addition to HCN and DCN, since DCO^+ and N_2D^+ are chemically coupled to these precursor species.

The effect of turbulence is twofold. First, it transports ices to the disk surface, where the ices are thermally desorbed and photodissociated. Secondly, it transports H atoms and radicals from the disk surface to the midplane, where they contribute to grain-surface reactions. In the static model, CO is efficiently converted to CO_2 via the grain-surface reaction of $CO + OH$ in the layer above the CO snow surface (§3.1). In the model with diffusion, on the other hand, CO is more abundant in this layer, since CO ice in the midplane is transported to this layer and sublimated, while CO_2 ice is transported to the disk surface to be photodissociated. Thus the column density of gaseous CO is slightly higher in the models with diffusion at $r \gtrsim 60$ au. In the midplane at $10 \text{ au} \lesssim r \lesssim 50$ au, on the other hand, CO is more efficiently converted to CO_2 ($\alpha = 10^{-3}$) and CH_3OH ($\alpha = 10^{-2}$) in the models with diffusion, due to the enhanced abundances of OH and H atoms. Inside a radius of ~ 40 au, HCO^+ is mostly on the disk surface, and is increased by the diffusion of CO in the turbulent disk.

The major nitrogen carriers are N_2 and NH_3 in our models. In the models with diffusion, the N_2 column density is reduced at $r \gtrsim 50$ AU, while it is enhanced at smaller radii, compared with the model without diffusion. In the cold outer midplane region, NH_3 is more efficiently formed via H atoms coming from the disk surface, while in the inner warm regions, midplane temperatures are too warm to (re)form NH_3 via grain-surface hydrogenation, and NH_3 is transported to the disk surface to be photodissociated (Furuya & Aikawa 2014). The high abundance of N_2 in the midplane enhances the abundance of N_2H^+ at $10 \text{ au} \lesssim r \lesssim 50$ au.

Diffusion of CO ice from the midplane and of H atoms from the disk surface enhance the abundances of hydrocarbons around and below the CO snow surface, and thus HCN and DCN, as well. Inside a radius of a few au, HCN and DCN abundances in the midplane are significantly reduced by the vertical mixing. Turbulence transports the large hydrocarbons, which represent the major carbon reservoir near the midplane of the static model, to the disk surface, and O atoms to the midplane, which destroys C-bearing species.

The vertical diffusion also affects the deuterium chemistry. First, it makes the depletion of HD in the midplane and conversion to HDO and NH_2D ices (see Appendix B) less efficient via the transport of the deuterated ices to the disk surface, where they can be dissociated. Thus in the model with mixing, HD and D atoms are more abundant in the midplane at $r \gtrsim 40$ au. Secondly, D atoms are transported towards the midplane and enhance deuteration via reactions such as (4).

3.5. Cosmic-ray Ionization

So far we have assumed that cosmic rays provide a minimum ionization rate of $5 \times 10^{-17} \text{ s}^{-1}$ in the midplane, where X-ray penetration is significantly attenuated. But the cosmic rays may be excluded by stellar winds with magnetic fields (e.g. Umebayashi & Nakano 1981; Cleeves et al. 2013a). In order to check the effect of the exclusion of cosmic rays, we investigated the model without cosmic-ray ionization. Here, the model disk is ionized by stellar X-rays, which dominate in and above the molecular layer, and the decay of radioactive nuclei, which sets a minimum ionization rate of $1 \times 10^{-18} \text{ s}^{-1}$ in the midplane (below the lower dotted line in Figure 12), given the ^{26}Al abundance derived from the analysis of meteorites for the formation stage of the Solar System (Umebayashi & Nakano 2009). Although the ionization rate could be smaller depending on the abundances of radioactive nuclei and the surface density of the disk (Umebayashi & Nakano 2009; Cleeves et al. 2013b), the effect of a low ionization rate is already apparent in the model presented here, and it is straightforward to extrapolate the results to an even lower ionization rate, at least qualitatively.

Figure 12 shows the distributions and column densities of HCO^+ , N_2H^+ , HCN and their deuterated isotopologs at $t = 3 \times 10^5 \text{ yr}$. The solid lines depict the column density in the model without cosmic-ray ionization, while the dashed lines depict our fiducial model. It is natural that the abundances of ionic molecules are suppressed by the low ionization rate. It should be noted that the dependence of molecular ion column densities on cosmic-ray ionization rate would vary among disk models. In the model with dark cloud dust, the midplane abundances of these molecular ions are lower due to the more efficient freeze-out of C-bearing and N-bearing molecules, and thus the X-ray dominated layer contributes more to the column density than in the model with mm-sized grains. Thus the decline of molecular ion column densities due to the exclusion of cosmic rays would be less significant in the disks with dark cloud dust. We found that the column density of HCO^+ in the model without cosmic-ray ionization, for example, is similar to that in Figure 8 in the dark cloud dust model. The column density of DCO^+ , on the other hand, is reduced by about an order of magnitude at $10 \text{ au} \lesssim r \lesssim 100 \text{ au}$ compared with Figure 8.

Comparing the right column in Figure 12 with that in Figure 5, we can see that both HCN and DCN are reduced in the outer ($r \gtrsim 10 \text{ au}$) midplane in the model without cosmic-ray ionization. Cosmic rays play a key role in forming N atoms and hydrocarbons such as CH_3 from N_2 and CO, respectively. N atoms are formed by the recombination of N_2H^+ with a small branching ratio, which is produced by protonation of N_2 . CO reacts with He^+ to form C^+ , which goes through successive reactions with H_2 and electrons to form hydrocarbons. Inside a radius of $\sim 3 \text{ au}$, on the other hand, column densities of HCN and DCN are slightly higher in the model without cosmic rays than in Figure 5, since the production of O atoms,

which destroy them, from water and CO₂ is suppressed by the low ionization rate. In the disk with dark cloud dust, both HCN and DCN are mostly abundant in the warm X-ray dominated layers, and thus their column densities do not depend much on the midplane ionization rate, except at $r \lesssim 3$ au, where DCN is more abundant in the model without cosmic rays.

4. Discussion

The motivation of the present work is to investigate the major deuteration paths and their efficiency in disk models with an updated gas-grain chemical network, rather than constructing a best fit model for a specific object. It is, however, worth comparing our model results with recent observations of deuterated species and their normal isotopologs. Table 2 summarizes the morphologies of integrated intensity maps of H¹³CO⁺, DCO⁺, N₂H⁺, N₂D⁺, H¹³CN, and DCN in two full disks around T Tauri stars (AS 209 and IM Lup), two transition disks around T Tauri stars (V4046 and LkCa 15) and two disks around Herbig Ae stars (MWC 480 and HD 163296). It is mainly based on Huang et al. (2017), and is supplemented by Öberg et al. (20011), Huang & Öberg (2015), Salinas et al. (2017), and Flaherty et al. (2017). Comparison should be qualitative, rather than quantitative, since disk physical structures are expected to vary among objects, including the radial distribution of midplane temperature, which sets the location of the CO snow line. While we compare the distribution of molecular lines with the estimated position of the CO snow line and temperature distribution for some disks, the derivation of temperature distributions in disks is not straightforward due to the opacity effect and temperature gradient in the vertical direction. CO sublimation temperature, and thus the position of CO snow line could also depend on the ice composition, i.e. whether its surface is water-rich or not, while desorption energy of a molecule is set to be constant in our model. It should also be noted that we compare the radial profiles (distributions) of molecular column density in our models with the observed distributions of line emissions. Huang et al. (2017) observed the $J = 3 - 2$ emission lines of DCO⁺, DCN, H¹³CO⁺, and H¹³CN, while Huang & Öberg (2015) observed the $J = 3 - 2$ line of N₂D⁺. Using the RADEX code (van der Tak et al. 2007), we estimate that the opacity of the $J = 3 - 2$ emission lines of HCO⁺, DCO⁺, N₂H⁺ and HCN reaches unity, when the molecular column density is a few 10¹² cm⁻², with a gas temperature of 30 K. These emission lines from our model disks are thus expected to be optically thin except for limited regions where the molecular column densities have a peak; the radial profile of the emission (e.g. ring emission) basically reflects the column density distributions.

4.1. Molecular Ions

In IM Lup, DCO^+ emission shows a double-ring structure with radii of 110 au and 310 au, while H^{13}CO^+ has a single ring structure located at ~ 130 au. Öberg et al. (2015) attributed the H^{13}CO^+ ring and the inner ring of DCO^+ to the CO snow line. The central dip (i.e. a small region of low brightness) in the molecular emission lines is suggested to be caused by the subtraction of the optically thick dust continuum. Thus we cannot tell if H^{13}CO^+ and DCO^+ decrease inwards at $r \lesssim 95$ au. The location of the DCO^+ outer ring coincides with the edge of the disk observed in the millimeter continuum. Öberg et al. (2015) argued that in this outermost radius the dust opacity is reduced, which enhances the photodesorption of CO and thus the DCO^+ abundance. Our model with mm-sized grains is consistent with this observation. The HCO^+ and DCO^+ column density increases inwards around (slightly outside) the CO snow line. Beyond the CO snow line, on the other hand, the DCO^+ column density increases outwards, as in the outer ring in IM Lup, although desorption via cosmic-rays is more efficient than photodesorption in the cold midplane in our model.

Another T Tauri disk, AS 209, shows more compact emission of H^{13}CO^+ and DCO^+ than does IM Lup. While H^{13}CO^+ shows a ring of $r \sim 50$ au, the radial size of the DCO^+ emission is similar to or slightly extended than 90 au, at which continuum emission shows a break. DCO^+ also has a central dip, which is shallower than that of H^{13}CO^+ (Huang et al. 2017). The midplane dust temperature distribution is estimated from continuum observations (Andrews et al. 2009); it is about 20 K at $r \sim 60$ au. Hence the ring-like emission of H^{13}CO^+ could coincide with the CO snow line. Our models indicate that DCO^+ inside the CO snow line could be formed via reactions (4) and $\text{CH}_4\text{D}^+ + \text{CO}$. Perez et al. (2012) found that the dust opacity index β increases outwards, which suggests that grains have grown (at least) to mm-sizes inside 80 au, while grains are still small at the outer radius. The absence of an outer DCO^+ ring could be due to efficient freeze out (and chemical conversion) of CO molecules on small dust grains. C^{18}O emission, however, shows a local peak at $r \sim 150$ au, indicating enhanced non-thermal desorption of CO there (Huang et al. 2016). It is not straightforward, either, to explain in our model why the central dip of H^{13}CO^+ is more clear than that of DCO^+ . Although the HCO^+ abundance in the midplane could decline at small radii due to a low ionization degree, or sublimation of H_2CO , H_2S and H_2O , which have higher proton affinities than CO, HCO^+ is the dominant charge carrier at the disk surface, which makes the distribution of HCO^+ column density relatively flat. In our model with CO and H_2O depletion, the HCO^+ column density shows a ring-like structure with a depression at $r \lesssim$ a few au, which indicates that the disk surface might be deficient in carbon at the dip radius. A disk structure model specific for AS 209 and a chemical model with isotope selective CO photodissociation might also be necessary to account for the central dip of

H^{13}CO^+ .

In addition to HCO^+ , N_2D^+ is detected in AS 209. Its emission is offset from the disk center, and has a peak around the outer edge of the ^{13}CO emission, which is consistent with our models.

LkCa15 is a transient disk with a central hole of 40 – 50 au in the dust continuum. Distributions of H^{13}CO^+ and DCO^+ emission in LkCa15 are qualitatively similar to those in IM Lup; the H^{13}CO^+ emission is rather compact, peaking at ~ 40 au, while the DCO^+ emission is more extended than the dust disk of radius ~ 200 AU, although the ring-like structure is much less clear in LkCa 15. Piétu et al. (2006) derived a disk temperature of 22 ± 1 K at $r = 100$ au. Thus DCO^+ emission comes from both inside and outside the CO snow line. The ring of H^{13}CO^+ emission, on the other hand, could be linked to the hole seen in the dust continuum.

Another transient disk, V4046, has a central hole of radius ~ 29 au in the dust continuum. While H^{13}CO^+ emission is diffuse extending to ~ 200 au, DCO^+ emission has a ring-like structure with its peak at ~ 70 au (Huang et al. 2017). Rosenfeld et al. (2012) estimated the temperature distribution to be $T(r) = 115(r/10\text{au})^{-0.63}$ K; i.e. the temperature is 27 K at $r = 100$ au. The DCO^+ ring thus could be caused by reactions (4) and $\text{CH}_4\text{D}^+ + \text{CO}$. It is consistent with our model that the H^{13}CO^+ distribution is rather flat and extends inwards compared with that of DCO^+ . Rosenfeld et al. (2013) determined that most of the dust mass is confined to a ring with a peak at $r = 37$ au and FWHM of 16 au. The disk may not extend beyond the CO snowline, where DCO^+ could have another (outer) emission peak.

In MWC 480, both H^{13}CO^+ and DCO^+ emissions have a peak at ~ 40 au (Huang et al. 2017). Despite the relatively high luminosity of the central star ($11.5 L_\odot$), the disk temperature is rather low. Piétu et al. (2006) constrained the disk temperature to be ~ 20 K at a radius of 20 – 30 au. Akiyama et al. (2013) observed ^{12}CO ($J = 3 - 2$), ^{12}CO ($J = 1 - 0$) and ^{13}CO ($J = 1 - 0$), and estimated a gas temperature of $\sim 13 - 15$ K for the layer traced by ^{13}CO ($J = 1 - 0$) at the radius of 100 au. HCO^+ and DCO^+ emission thus seems to originate in the region around and slightly outside the CO snow line.

In HD 163296, the H^{13}CO^+ ($J = 3 - 2$) line features an emission ring peaking at $r \sim 50$ au, and also has a more extended component with a break at $r \sim 200$ au. The DCO^+ emission shows a rather broad ring with a peak at $r \sim 70$ au (Huang et al. 2017). The temperature distribution in the disk of HD 163296 was derived by Isella et al. (2016) from CO observations; the midplane temperature is 23 K at $r \sim 80$ au. Qi et al. (2015), on the other hand, derived the location of the CO snow line to be $r \sim 90$ au from observations

of N_2H^+ and CO isotopologs. HCO^+ and DCO^+ emission thus originates both inside and outside of the CO snow line. Recently, Salinas et al. (2017) reported spatially resolved emissions of DCO^+ , N_2D^+ , and DCN. Their analysis shows that DCO^+ emission can be divided to three ring-like components at 70 au, 150 au, and 260 au (see also Flaherty et al. 2017). The innermost and second ring coincide with the emission peaks of DCN and N_2D^+ , respectively, while the outermost ring could arise from the non-thermal desorption of CO, as in the outer ring of IM Lup (Salinas et al. 2017). In our fiducial model, the radial distribution of the DCO^+ column density can be divided to three components at $r \sim$ several au, 10-30 au, and an outermost radius ($\gtrsim 100$ au). The innermost peak coincides with the local peak of DCN, while DCO^+ originates in non-thermal desorption of CO in the midplane at the outermost radius, which could be consistent with Salinas et al. (2017). The second component at $r \sim 10 - 30$ au, however, is located inside the local peak of the N_2D^+ column density ($\gtrsim 20 - 100$ au).

So far, the DCO^+ emission detected in disks always has a central hole or dip (Huang et al. 2017; Qi et al. 2015). In our models, the DCO^+ distribution does have a dip. Right outside the dip, DCO^+ is mainly formed by reaction (4), while D atoms are destroyed mainly by the reaction with HS inside the dip. Although the sublimation of S-bearing species such as H_2S seems to be a key for the decline of D atom in our model, a derivation of the physical condition for the decline of D atoms and thus of DCO^+ may not be straightforward, since D atoms are chemically active. It should also be noted that a central dip could be caused by subtraction of optically thick dust continuum, rather than by a chemical effect, in some disks (Huang et al. 2017; Salinas et al. 2017).

4.2. HCN and DCN

In our models, both in models with mm-sized dust and dark cloud dust, the radial distributions of the HCN and DCN column densities are centrally peaked, although the DCN/HCN ratio is low ($10^{-5} - 10^{-4}$) at the central region ($r \lesssim 10$ au) due to high temperature. Their column densities drop sharply outside this high temperature region, and then slightly increase outwards, with the gradient steeper for DCN. In the models with vertical diffusion, the central peak disappears, since hydrocarbons, from which HCN and DCN are formed, are transported to the disk surface to be destroyed.

In the disk of IM Lup, H^{13}CN is not detected and DCN emission is weak and diffuse (Huang et al. 2017), while both H^{13}CN and DCN are clearly detected and have a central dip (Huang et al. 2017) in the disk of AS 209. In these disks, HCN and DCN are not centrally peaked, possibly because the temperature is not high enough to desorb HCN at

the radius traced by current observations (beam size of ~ 60 au), or because turbulent mixing is at work. V4046 and HD163296, on the other hand, show centrally peaked H^{13}CN emission and a central dip in DCN emission. If these features simply reflect their column density distributions, it is difficult to account for in our fiducial model, in which both HCN and DCN are most abundant in the innermost radii. Our models with turbulent diffusion, however, might produce the observed feature; while DCN is abundant only in the outer cold regions, HCN is abundant at the disk surface even inside 20 au, which could be bright due to high temperatures.

5. SUMMARY

We investigated deuterium chemistry coupled with the nuclear spin-state chemistry of H_2 and H_3^+ and their isotopologs in protoplanetary disks. Our principal findings are as follows:

1. We have found multiple paths for deuterium enrichment. The exchange reactions with D atoms, such as $\text{HCO}^+ + \text{D}$, are found to be effective, in addition to $\text{H}_3^+ + \text{HD}$, $\text{CH}_3^+ + \text{HD}$, and $\text{C}_2\text{H}_2^+ + \text{HD}$, which had been considered in previous studies.
2. As discussed in Appendix A, the OPR of H_2 is found to be almost thermal, as long as the cosmic rays ionize the disk with a rate $\sim 10^{-17} \text{ s}^{-1}$. In the cold (~ 10 K) midplane, however, the OPR reaches its minimum value, which is higher than the thermal value. The minimum value is determined by the balance between the rates of H_2 formation, which sets the OPR to be 3, and spin conversion via ion-molecule reactions involving protons and H_3^+ mainly. The OPR could reach the thermal value at such cold dense regions, if we take into account the spin conversion on grain surfaces, which has recently been found in laboratory experiments (Ueta et al. 2016). We have also analyzed the OPR of H_3^+ and H_2D^+ , and the abundances of H_2D^+ , DCO^+ , and N_2D^+ in the cold midplane, in part by the use of derived analytical formulae.
3. In our models, the contribution of the exchange reaction $\text{CH}_3^+ + \text{HD}$ is found to be less significant than that described in Favre et al. (2015). The increasing OPR of H_2 helps the backward reaction at $T \gtrsim 20$ K.
4. In the disk model with mm-sized grains, reduced freeze-out rates enhance the gaseous molecular abundances in the cold midplane. DCO^+ , N_2D^+ , and DCN in the outer midplane thus contribute significantly to their column densities. The radial distribution of the DCO^+ column density has a double-ring structure, similar to the DCO^+ emission

observed in IM Lup. While the outer ring is caused by the enhanced deuteration of H_3^+ and less efficient chemical conversion of HD and CO in the outer radii in our model, the inner ring is linked to the CO snow line and depletion of D atoms due to reactions with HS for example. N_2D^+ , on the other hand, is more abundant outside the CO snow line. Gaseous DCN decreases inward, except in the central hot region ($T \gtrsim 100$ K) where it is thermally desorbed.

5. If the elemental C/O ratio is higher than unity due to sedimentation of H_2O ice, hydrocarbons become abundant. The exchange reaction $\text{CH}_3^+ + \text{HD}$, which eventually leads to the ion CH_4D^+ , thus contributes to form DCO^+ via the reaction $\text{CH}_4\text{D}^+ + \text{CO}$ in the warm molecular layer. The column densities of gaseous HCN and DCN are also enhanced by an order of magnitude compared with the fiducial model. The spatial distributions of molecular abundances and radial profiles of molecular column densities are, however, qualitatively similar to those in our fiducial model.
6. In the disk model with dark cloud dust, the freeze out of molecules is more severe in the outer midplane, while the disk surface is better shielded from UV radiation than in the model with mm-sized grains. The disk surface area thus harbors abundant gaseous molecules and contributes to the column densities (and emissions) of HCO^+ , DCO^+ , N_2H^+ , HCN and DCN. One exception is N_2D^+ , which is not abundant in the disk surface.
7. Turbulence helps to prevent chemical conversion of molecules to less volatile species by transporting ices from the midplane to the disk surface, where ices are desorbed and photodissociated, but it also enhances the formation of saturated or less volatile molecules in the midplane by transporting H atoms and radicals from the disk surface. For example, NH_3 ice formation is hampered and thus N_2 and N_2H^+ abundances tend to be enhanced inside the N_2 snow line. Turbulence also transports D atoms in the disk surface to the lower layers, which helps the formation of DCO^+ and N_2D^+ . At the innermost radii, the abundances of HCN and DCN are significantly reduced by the turbulence; their icy components and hydrocarbons are transported to the disk surface and destroyed, while O atoms are transported to the midplane to react with C-bearing species.
8. If the penetration of cosmic rays is hampered by the stellar wind, the midplane ionization rate decreases by more than one order of magnitude. Column densities of molecular ions decline, although the decrement varies with radius, species, and the dust grain sizes in the disk model. HCN and DCN also decrease at $r >$ several au, since the cosmic-ray ionization is needed to form their precursors, N atoms and hydrocarbons, from N_2 and CO, respectively.

This work is supported by JSPS KAKENHI Grant Numbers 23540266, 16H00931, and 17K14245. We would like to thank Hideko Nomura for providing the disk physical models, and to Jane Huang, Megumi Kayanuma, and Liton Majumdar for helpful discussions. We are grateful to the anonymous referee for helpful comments, which improved the manuscript. E. H. wishes to acknowledge the support of the National Science Foundation through grant AST-1514844.

A. H₂ OPR

In our chemical reaction network, the OPR is assumed to be 3 for newly formed H₂ molecules on grain surfaces. Neglecting rapid thermalization on the grain, they are desorbed into the gas phase, where the spin state changes via proton exchange reactions with ions such as H₃⁺. Figure 13 (a) shows the 2D distribution of gas temperature, and Figure 13 (b) shows the 2D distribution of the H₂ OPR at $t = 3 \times 10^5$ yr in our fiducial model. The distribution is the same at $t = 1 \times 10^5$ yr, 3×10^5 yr and 9.3×10^5 , because the H₂ OPR reaches steady state on a relatively short timescale ($< 10^5$ yr). In Figure 13 (a) and (b) the horizontal axis (r) is shown in linear scale, since we discuss only the low temperature regions in this Appendix. The OPR apparently follows the gas temperature distribution. In order to study the dependence of OPR on gas temperature more quantitatively, we plot the OPR as a function of gas temperature in Figure 13 (c). At low temperatures (\lesssim several tens of K), where only the lowest two rotational levels need be considered, the OPR is mostly equal to the value of thermal equilibrium,

$$n(\text{o-H}_2)/n(\text{p-H}_2) = 9 \exp(-170.5/T), \quad (\text{A1})$$

which is depicted by the solid line, while at higher temperatures the OPR asymptotically reaches the statistical equilibrium value of 3. At $T \sim 10$ K, however, the OPR obtained in the numerical calculation reaches minimum value, which is higher than the thermal value. The minimum value can be explained as follows.

The steady state value of the H₂ OPR is given by

$$\begin{aligned} \text{OPR}_{\text{st}} &= \frac{\beta_1 + b_0\beta_2}{1 + (1 - b_0)\beta_2} \\ \beta_1 &= \tau_{\text{op}}/\tau_{\text{po}} \\ \beta_2 &= \tau_{\text{op}}/\tau_{\text{H}_2}, \end{aligned} \quad (\text{A2})$$

where b_0 ($= 0.75$) is the branching ratio to form o-H₂ for H₂ formation on grains, τ_{H_2} is the timescale of H₂ formation, and τ_{op} and τ_{po} represent the timescale of spin conversion via

proton exchange from ortho to para and from para to ortho, respectively (e.g. Furuya et al. 2015). When the abundance of ions such as H_3^+ is high enough, β_1 dominates in (A2), and the OPR reaches the thermal value. If the ion abundance is low, on the other hand, the OPR is determined by β_2 ; i.e. the balance between the H_2 formation, which sets the OPR to 3, and the spin conversion via ion-molecule reactions. In the disk model, the low temperature ($T \sim 10$ K) region corresponds to the outer midplane; due to the low ionization degree, the OPR is set by β_2 :

$$\beta_2 = \frac{\pi a^2 \sqrt{\frac{2kT}{\pi m}} n(\text{grain}) n(\text{H})}{k_{\text{op}} n(\text{XH}^+) n(\text{H}_2)}, \quad (\text{A3})$$

where k is the Boltzmann constant, m is the mass of a hydrogen atom, $n(\text{XH}^+)$ is the number density of ions which convert ortho- to para- H_2 through proton exchange reactions with a rate coefficient k_{op} . Considering the balance between the formation and destruction of H_2 , the numerator, i.e. the formation rate of H_2 , can be replaced by the H_2 destruction rate via cosmic-ray/X-ray ionization;

$$\beta_2 = \frac{\zeta n(\text{H}_2)}{k_{\text{op}} n(\text{XH}^+) n(\text{H}_2)} = \frac{\zeta}{k_{\text{op}} n(\text{XH}^+)}, \quad (\text{A4})$$

where ζ is the H_2 ionization rate. Then the minimum value is almost equivalent to the OPR given by Walmsley et al. (2004). It should also be noted that the minimum value of OPR in our disk model is much lower than $\sim 10^{-3}$, which is often assumed in the model of molecular clouds (e.g. Flower et al. 2006; Faure et al. 2013), because $n(\text{XH}^+)$ in eq. (A4) depends on the ionization rate and gas density.

Recent laboratory experiments found that the OPR of H_2 is thermalized via the spin conversion on amorphous water ice (Ueta et al. 2016). The conversion rate is higher than the desorption rate at $\lesssim 12$ K. Thus OPR could reach the thermal value even at 10 K, if we include the conversion on grain surfaces.

Figure 13 (c) shows that there are some deviations of the H_2 OPR from the thermal value at warm temperatures ($T \gtrsim 25$ K), as well. Such deviations are caused by the relatively low ionization degree in the warm dense midplane. The OPR cannot simply be calculated from β_2 (eq. A4) in these regions, since β_1 and β_2 are comparable, unlike the low temperature limit ($T \sim 10$ K) discussed above.

Finally it should be noted that, in the model without cosmic-ray ionization, the region with non-thermal H_2 OPR extends both in the radial and vertical directions (Figure 13 (d)). The ionization rate is too low around the midplane for β_1 to dominate in equation (A2).

B. Analytical formula of the OPR values and abundances of molecular ions in the outer midplane

In §3, we showed that the major formation paths of deuterated molecular ions vary spatially. It is thus difficult to derive analytical formulae of abundances of these ions which are applicable to the whole disk. Derivation of the analytical formulas is possible, however, if we restrict ourselves to the cold outer midplane. Since molecules such as H_2D^+ and N_2D^+ have their peak abundances in the outer midplane, and since they are often considered to be tracers of ionization degree, the analytical formulae could be useful.

First, we derive the OPR of H_3^+ . The analytical formula for the H_3^+ abundance is given in eq (18) in Aikawa et al. (2015); it is determined by the formation via cosmic-ray/X-ray ionization of H_2 and the destruction by reactions with CO, N_2 , electrons, and negatively charged grains. Its spin state changes via reactions with H_2 (Oka 2004):

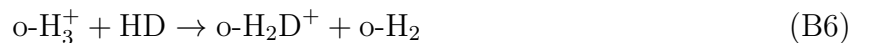


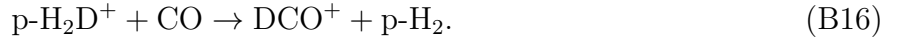
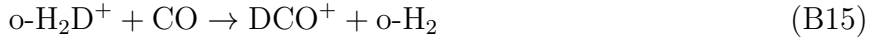
The OPR of H_3^+ is thus given at steady state by

$$\frac{n(\text{o-H}_3^+)}{n(\text{p-H}_3^+)} = \frac{(k_{\text{B3}} + k_{\text{B4}})n(\text{o-H}_2)}{k_{\text{B1}}n(\text{p-H}_2) + k_{\text{B2}}n(\text{o-H}_2)}. \quad (\text{B5})$$

Figure 14 (a) shows the H_3^+ OPR in our fiducial disk model (green crosses) and the value given by equation (B5) (red line). We fix the H_2 OPR of (A1) and its minimum value of 1×10^{-5} , for simplicity. We see reasonable agreement between (B5) and the OPR of H_3^+ in the numerical calculation, while there are some deviations at $T \gtrsim 25$ K, which originate from the non-thermal OPR of H_2 (Figure 13 c). The deviation stands out in Figure 14 (a), in which the vertical axis is shown in linear scale, while it is shown in logarithmic scale in Figure 13 (c).

The major formation and destruction paths of H_2D^+ are

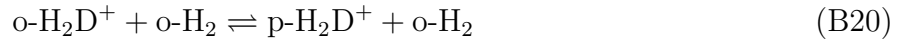
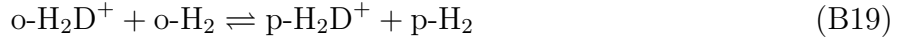
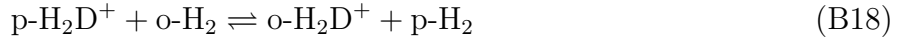




The balance between these reactions is described as

$$\begin{aligned} n(\text{HD})\{k_{B6}n(\text{o-H}_3^+) + (k_{B7} + k_{B8} + k_{B9})n(\text{p-H}_3^+)\} = & \quad (\text{B17}) \\ & n(\text{o-H}_2)\{k_{B10}n(\text{o-H}_2\text{D}^+) + (k_{B11} + k_{B12})n(\text{p-H}_2\text{D}^+)\} \\ & + (k_{B13} + k_{B15})n(\text{o-H}_2\text{D}^+)n(\text{CO}) + (k_{B14} + k_{B16})n(\text{p-H}_2\text{D}^+)n(\text{CO}). \end{aligned}$$

The spin state of H_2D^+ is converted via



in a shorter timescale than that of $\text{H}_2\text{D}^+/\text{H}_3^+$ conversion. The o/p ratio of H_2D^+ can thus be described by

$$\frac{n(\text{o-H}_2\text{D}^+)}{n(\text{p-H}_2\text{D}^+)} = \frac{(k_{B18}^+ + k_{B20}^-) \times n(\text{o-H}_2)/n(\text{p-H}_2) + k_{B19}^-}{(k_{B19}^+ + k_{B20}^+) \times n(\text{o-H}_2)/n(\text{p-H}_2) + k_{B18}^-} \quad (\text{B21})$$

(Gerlich et al. 2002; Brünken et al. 2014). The H_2D^+ abundance is then given by

$$n(\text{H}_2\text{D}^+) = \frac{n(\text{HD})\{k_{B6}n(\text{o-H}_3^+) + (k_{B7} + k_{B8} + k_{B9})n(\text{p-H}_3^+)\}}{k_{B10}n(\text{o-H}_2)^{\frac{x}{x+1}} + (k_{B11} + k_{B12})n(\text{o-H}_2)^{\frac{1}{x+1}} + (k_{B13} + k_{B15})n(\text{CO})}, \quad (\text{B22})$$

where x is the o/p ratio of H_2D^+ (B21). Note that the rate coefficient of $\text{H}_2\text{D}^+ + \text{CO}$ is the same for $\text{o-H}_2\text{D}^+$ and $\text{p-H}_2\text{D}^+$. If the H_2D^+ abundance derived above is comparable to that of main isotopolog, H_3^+ , it should be replaced by

$$n(\text{H}_2\text{D}^+) = n(\text{H}_3^+) \frac{n'(\text{H}_2\text{D}^+)}{n(\text{H}_3^+) + n'(\text{H}_2\text{D}^+)}, \quad (\text{B23})$$

where $n'(\text{H}_2\text{D}^+)$ denotes the value obtained in (B22).

Reasonable agreement between the analytical value and the numerical results for the o/p ratio of H_2D^+ is found in Figure 14 (b). In our numerical models, multiply-deuterated H_3^+

becomes more abundant than H_2D^+ in the outermost ($r \gtrsim 250$ au) midplane. The analysis of multi-deuterated species is, however, beyond the scope of this paper. Since we neglect the multiply deuterated isotopologs of H_3^+ , H_2D^+ represents the total deuterated- H_3^+ in our analysis. In the following, we therefore compare the analytical value of the H_2D^+ abundance with the sum of the abundances of deuterated H_3^+ ($n(\text{D}_3^+)/n_{\text{H}} + n(\text{D}_2\text{H}^+)/n_{\text{H}} + n(\text{H}_2\text{D}^+)/n_{\text{H}}$) obtained in our fiducial model. Figure 14 (c) shows the sum of deuterated H_3^+ abundance in our fiducial model (green), which is compared with the analytical value (red). At warm regions ($T \gtrsim 20$ K), the abundances of H_3^+ and its deuterated isotopologs are not simple functions of temperature; they depend on abundances of other species such as CO, N_2 and electrons (Aikawa et al. 2015). We use the latter abundances from our fiducial model in the calculation of the analytical formula of H_2D^+ abundance. Equation (B22) also needs the abundance of HD as an input. While its canonical value is 1.5×10^{-5} , HD abundance is decreased down to $\sim 10^{-7}$ via conversion to D-bearing ices such as NH_2D and HDO in the cold midplane in our numerical model (see also Sipilä et al. 2013; Teague et al. 2015). We thus use the HD abundance from our fiducial model, as well.

Figures 15 (a) and (b) show the 2D distribution of deuterated H_3^+ in our fiducial model, and the H_2D^+ abundance derived from eq. (B22), respectively. We can see a reasonable agreement between the numerical model and the analytical formula. For a comparison, Figure 15 (c) shows the distribution of H_2D^+ abundance derived from eq. (B22) assuming that CO, N_2 and HD are not converted to other molecules; HD abundance is set to be constant ($n(\text{HD})/n_{\text{H}} = 1.5 \times 10^{-5}$), and CO and N_2 abundances are determined simply by the balance between adsorption and desorption (Aikawa et al. 2015). H_2D^+ abundance is higher than the numerical model, mainly due to a higher HD abundance.

Once we obtain the analytical formula of the H_2D^+ abundance, we can calculate the DCO^+ and N_2D^+ abundances, by simply replacing H_3^+ with H_2D^+ and modifying the corresponding reaction rate coefficients in equations (22) and (21) in Aikawa et al. (2015). The resultant 2D distributions are shown in Figure 15 (d-i). Panels (e) and (h) show distributions of DCO^+ and N_2D^+ , respectively, derived from the analytical formulas using the abundances of HD, CO, N_2 , and electrons from our fiducial model, while the abundances of HD, CO and N_2 are given analytically for panels (f) and (i). The agreements between the numerical model (panels d and g) and analytical values (panels e and h) confirm that DCO^+ and N_2D^+ are mainly formed via deuterated H_3^+ in the outer midplane.

REFERENCES

Adams, N. G. & Smith, D. 1985, ApJ, 294, L63

Table 1: Initial abundances of major species

species	abundance
N	1.8 (-8) ^a
O	8.8 (-9)
o-H ₂	1.6 (-3)
p-H ₂	5.0 (-1)
HD	1.3 (-5)
CO	6.2 (-5)
CH ₄	7.4 (-6)
H ₂ CO	3.5 (-6)
CO ₂	2.6 (-6)
CH ₃ OH	8.8 (-7)
N ₂	3.8 (-6)
HCN	2.0 (-7)
DCN	7.7 (-9)
NH ₃	1.7 (-5)
NH ₂ D	2.0 (-7)
H ₂ O	1.1 (-4)
HDO	8.5 (-8)

^a $a(b)$ means $a \times 10^b$.

- Aikawa, Y., Miyama, S. M., Nakano, T., & Umebayashi, T. 1996, *ApJ*, 467, 684
- Aikawa, Y., Umebayashi, T., Nakano, T. & Miyama, S. M. 1997, *ApJ*, 486, L51
- Aikawa, Y. & Herbst, E. 1999, *ApJ*, 526, 314
- Aikawa, Y., Umebayashi, T., Nakano, T., & Miyama, S.M. 1999, *ApJ*, 519, 705
- Aikawa, Y. & Nomura, H. 2006, *ApJ*, 642, 1152
- Aikawa, Y., Wakelam, V., Hersant, F., Garrod, R.T. & Herbst, E. 2012, *ApJ*, 760, 40
- Aikawa, Y., Furuya, K., Nomura, H. & Qi, C. 2015, *ApJ*, 807, 120
- Akiyama, E., Momose, M., Kitamura, Y. et al. 2013, *PASJ*, 65, id. 123
- Albertsson, T., Semenov, D., & Henning, Th. 2014, *ApJ*, 748, 39
- Altwegg, K., Balsiger, H., Bar-Nun, A. et al. 2015, *Science*, 347, id. 1261952
- Andrews, S. M., Wilner, D. J., Hughes, A. M., Qi, C., & Dullemond, C.P. 2009, *ApJ*, 700, 1502
- Bacmann, A., Lefloch, B., Ceccarelli, C. et al. 2003, *ApJ*, 585, L55
- Balbus, S.A. & Hawley, J. F. 1991, *ApJ*, 376, 214
- Bergin, E. A., Du, F., Cleeves, L. I. et al. 2016, *ApJ*, 831, 101
- Brünken, S., Sipilä, O., Chambers, E.T. et al. 2014, *Nature*, 516, 219
- Caselli, P., Stancheva, T., Shalabiea, O., Shematovich, V. I., & Herbst, E. 2002, *P&SS*, 50, 1257
- Caselli, P., Hasegawa, T.I., & Herbst, E. 1998, *ApJ*, 495, 309
- Caselli, P., van der Tak, F.F.S., Ceccarelli, C., & Bacmann, A. 2003, *A&A*, 403, L37
- Cazzaux, S. & Tielens, A.G.G.M. 2004, *ApJ*, 604, 222
- Cazzaux, S. & Tielens, A.G.G.M. 2010, *ApJ*, 715, 698
- Cleeves, L.I., Adams, F.C. , & Bergin, E. A., 2013, *ApJ*, 772, 5
- Cleeves, L. I., Adams, F.C., Bergin, E. A., & Visser, R. 2013, *ApJ*, 777, 28
- Cleeves, L. I., Bergin, E.A., Alexander, C.M.O'D. et al. 2014, *Science*, 345, 1590

- Cleeves, L. I., Bergin, E. A., & Adams, F. C. 2014, *ApJ*, 794, 123
- Cleeves, L.I., Bergin, E.A., Alexander, C.M. O’D. et al. 2016, *ApJ*, 819, 13
- Coutens, A., Vastel, C., Hincelin, U. et al. 2014, *MNRAS*, 445, 1299
- Draine, B.T. & Bertoldi, F. 1996, *ApJ*, 468, 269
- Du, F., Bergin, E. A., Hogerheijde, M. et al. 2017, *ApJ*, 842, 98
- Favre, C., Cleeves, L. I., Bergin, E. A., Qi, C., & Blake, G. A. 2013, *ApJ*, 776, L38
- Favre, C., Bergin, E. A., Cleeves, L. I. et al. 2015, *ApJ*, 802, L23
- Flaherty, K. M., Hughes, A. M., Rosenfeld, K. A. et al. 2015, *ApJ*, 813, 99
- Flaherty, K. M., Hughes, A. M., Rose, S. C. et al. 2017, *ApJ*, 843, 150
- Flower, D. R., Pineau des Forêts, & Walmsley, C. M. 2006, *A&A*, 449, 621
- Faure, A., Hily-Blant, P., Le Gal, R., Rist, C., & Pineau des Forêts 2013, *ApJ*, 770, L2
- Furuya, K., Aikawa, Y., Nomura, H., Hersant, F., & Wakelam, V. 2013, *ApJ*, 779, 11
- Furuya, K. & Aikawa, Y. 2014, *ApJ*, 790, 97
- Furuya, K., Aikawa, Y., Hincelin, U. et al. 2015, *A&A*, 584, A124
- Furuya, K., van Dishoeck, E. F., & Aikawa, Y. 2016, *A&A*, 586, A127
- Garrod, R.T. & Herbst, E. 2006, *A&A*, 457, 927
- Garrod, R.T., Wakelam, V., & Herbst, E. 2007, *A&A*, 467, 1103
- Geiss, J. & Gloeckler 1998, *SSRv*, 84, 239
- Gerlich, D., Herbst, E., & Roueff, E. 2002, *P&SS*, 50, 1275
- Harada, N., Herbst, E., & Wakelam, V. 2010, *ApJ*, 721, 1570
- Harada, N., Herbst, E., & Wakelam, V. 2012, *ApJ*, 756, 104
- Hasegawa, T.I. & Herbst, E. 1993, *MNRAS*, 261, 83
- Herczeg, G. J., Linsky, J. L., Valenti, J. A., Johns-Krull, C. M., & Wood, B. E. 2002, *ApJ*, 572, 310

- Hincelin, U., Herbst, E., Chang, Q. et al. 2014, 69th International Symposium on Molecular Spectroscopy, MF09
- Hogerheijde, M. R., Bergin, E. A., Brinch, C. et al. 2011, *Science*, 334, 338
- Huang, J., & Öberg, K.I. 2015, *ApJ*, 809, L26
- Huang, J., Öberg, K.I., & Andrews, S. 2016, *ApJ*, 823, L18
- Huang, J., Öberg, K.I., Qi, C. et al. 2017, *ApJ*, 835, 231
- Hugo, E., Asvany, O., Schlemmer, S. 2009, *J. Ch. Ph.*, 130, 164302
- Isella, A., Guidi, G., Testi, L. et al. 2016, *PRL*, 117, 251101
- Johansen, A. & Klahr, H. 2005, *ApJ*, 634, 1353
- Kama, M., Bruderer, S., van Dishoeck, E. F. et al. 2016, *A&A*, 592, 83
- Kamp, I. & Bertoldi, F. 2000, *A&A*, 353, 276
- Kastner, J. H., Huenemoerder, D. P., Schulz, N. S., Canizares, C. R., & Weintraub, D. A. 2002, *ApJ*, 567, 434
- Krijt, S., Ciesla, F. J., & Bergin, E. A., 2016, *ApJ*, 833, 285
- Li, X., Heays, A. N., Visser, R. et al. 2013, *A&A*, 555, A14
- Linsky, J.L. 2003, *SSRv*, 106, 49
- Mathews, G.S., Klaassen, P.D., Juhász, A. et al. 2013, *A&A*, 557, A132
- Meijerink, R., Pontoppidan, K. M., Blake, G.A., Poelman, D.R., & Dullemond, C. P. 2009, *ApJ*, 704, 1471
- Millar, T.J., Bennet, A, & Herbst, E. 1989, *ApJ*, 340, 906
- Minissale, M., Dulieu, F., Cazaus, S. & Hocuk, S. 2016, *A&A*, 585, A24
- Mumma, M.J. & Charnley, S.B. 2011, *ARAA*, 49, 471
- Noble, J.A., Theule, P., Borget, F. et al. 2013, *MNRAS*, 428, 3262
- Nomura, H. & Millar, T. 2005, *A&A*, 438, 923
- Nomura, H., Aikawa, Y., Tsujimoto, M., Nakagawa, Y., & Millar, T., 2007, *ApJ*, 661, 334

- Nomura, H., Tsukagoshi, T., Kawabe, R. et al. 2016, *ApJ*, 819, L7
- Öberg, K.I., van Dishoeck, E. F., & Linnartz, H. 2009, *A&A*, 496, 281
- Öberg, K.I., Qi, C., Fogel, K.J. et al. 2011, *ApJ*, 734, 98
- Öberg, K.I, Qi, C., Wilner, D. J., & Hogerheijde, M. R. 2012, *ApJ*, 749, 162
- Öberg, K.I., Furuya, K., Loomis, R. et al. 2015, *ApJ*, 810, 112
- Oka, T., 2004, *JMoSp*, 228, 635
- Penteado, E. M., Walsh, C. & Cuppen, H. M. 2017, *ApJ*, 844, 71
- Pérez. L. et al. 2012, *ApJ*, 760, L17
- Piétu, V., Dutrey, A., Guilloteau, S., Chapillon, E., & Pety, J. *A&A* 460, L43-L47
- Qi, C., Wilner, D.J., Aikawa, Y., Blake, G.A., & Hogerheijde, M. R. 2008, *ApJ*, 681, 1396
- Qi, C., Öberg, K.I., Andrews, S. M. et al. 2015, *ApJ*, 813, 128
- Roberts, H. & Millar, T.J. 2000, *A&A*, 361, 388
- Rosenfeld, K.A., Andrews, S. M., Wilner, D. J., & Stempels, H. C. 2012, *ApJ*, 759, 119
- Rosenfeld, K. A., Andrews, S. M., Wilner, D. J., Kastner, J. H., & McClure, M. K. 2013, *ApJ*, 775, 136
- Roueff, E., Gerin, M., Lis, D.C. et al. 2013, *J. Phys. Chem. A*, 117, 9959
- Ruaud, M., Wakelam, V. & Hersant, F. 2016, *MNRAS*, 459, 3756
- Salinas, V. N., Hogerheijde, M. R., Matthews, G. S. et al. 2017, *A&A*, 606, A125
- Schilke, P., Walmsley, C.M., Pineau des Forets, G. et al. 1992, *A&A*, 256, 595
- Schwarz, K. R., Bergin, E. A., Cleeves, L. I. et al. 2016, *ApJ*, 823, 91
- Sipilä, O., Caselli, P., & Harju, J. 2013, *A&A*, 554, A92
- Smith, D., Adams, N.G., & Alge, E. 1982, *ApJ*, 263, 123
- Teague, R., Semenov, D., Guilloteau, S. et al. 2015, *A&A*, 574, A137
- Teague, R., Guilloteau, S., Semenov, D. et al. 2016, *A&A*, 592, A49

- Tielens, A.G.G.M. & Hollenbach, D., 1985, ApJ, 291, 722
- Umebayashi, T., & Nakano, T. 1981, PASJ, 33, 617
- Umebayashi, T. & Nakano, T. 2009, ApJ, 690, 69
- Ueta, H., Watanabe, N., Hama, T. & Kouchi, A. 2016, PRL, 116, 253201
- van der Tak, F.F.S., Black, J.H., Schöier, F.L., Jansen, D.J., van Dishoeck, E.F. 2007, A&A 468, 627
- van Dishoeck, E.F., Thi, W. -F., & Zadelhoff, G.-J. 2003, A&A, 2003, 400, L1
- Vastel, C., Caselli, P., Ceccarelli, C. et al. ApJ, 645, 1198
- Visser, R., van Dishoeck, E. F., & Black, J. H. 2009, A&A, 503, 323
- Wolcott-Green, J. & Haiman, Z. 2011, MNRAS, 412, 2603
- Walmsley, C. M., Flower, D. R., & Forêts 2004, A&A, 418, 1035
- Weingartner, J. C. & Draine, B. T., 2001, ApJ, 548, 296
- Willacy, K. 2007, ApJ, 660, 441
- Xu, R., Bai, X.-N., & Öberg, K. I. 2017, ApJ, 835, 162
- Zhang, K., Bergin, E. A., Blake, G. A., Cleeves, L. I., Schwarz, K. R. 2017, NatAs, 1, 0130

Table 2: Observations morphologies of molecular lines intensities^a

Object	Class	H ¹³ CO ⁺	DCO ⁺	N ₂ H ⁺	N ₂ D ⁺	H ¹³ CN	DCN
IM Lup	full disk (T Tauri)	ring-like	multiple rings	offset ^b	-	ring-like ^c	extended? ^d
AS 209	full disk (T Tauri)	ring-like	ring-like	offset ^b	offset ^e	ring-like	ring-like
LkCa 15	transition disk (T Tauri)	ring-like	diffuse	-	-	compact? ^d	multiple rings? ^d
V4046 Sgr	transition disk (T Tauri)	diffuse	ring-like	offset ^b	-	centrally peaked	ring-like
MWC 480	Herbig Ae	ring-like	ring-like	-	-	centrally peaked	compact? ^d
HD 163296	Herbig Ae	multiple rings	multiple rings ^{f,g}	-	ring-like ^g	centrally peaked	ring-like

^aBased on Huang et al. (2017) unless otherwise stated.

^bÖberg et al. (20011)

^cH¹³CN is not detected. H¹²CN shows a ring-like feature.

^dDetected but not categorized in Huang et al. (2017) due to relatively low S/N.

^eHuang & Öberg (2015)

^fFlaherty et al. (2017)

^gSalinas et al. (2017)

Table 3: Rate coefficients of major reactions of deuterated molecular ions^a

reaction	rate coefficients [cm ³ s ⁻¹]
B1	$1.5 \times 10^{-9} \exp(-136/T)^b$
B2	$4.00 \times 10^{-10} \exp(0.19/T)$
B3	$3.46 \times 10^{-10} \exp(0.69/T)$
B4	$8.03 \times 10^{-10} \exp(-32.6/T)$
B6	$1.11 \times 10^{-9} \exp(-0.35/T)$
B7	$6.08 \times 10^{-10} \exp(1.08/T)$
B8	$4.93 \times 10^{-10} \exp(0.95/T)$
B9	$3.11 \times 10^{-10} \exp(0.71/T)$
B10	$1.64 \times 10^{-10} \exp(-6.31/T)$
B11	$9.32 \times 10^{-9} \exp(-94.6/T)$
B12	$1.48 \times 10^{-10} \exp(-58.8/T)$
B13	1.07×10^{-9}
B15	5.37×10^{-10}
B18 ⁺	$1.26 \times 10^{-9} \exp(-0.06/T)$
B18 ⁻	$5.58 \times 10^{-10} \exp(-82.7/T)$
B19 ⁺	$8.31 \times 10^{-11} \exp(0.92/T)$
B19 ⁻	$1.02 \times 10^{-9} \exp(-256/T)$
B20 ⁺	$1.68 \times 10^{-10} \exp(0.77/T)$
B20 ⁻	$6.04 \times 10^{-10} \exp(-88.8/T)$

^aOka (2004), Hugo et al. (2009), Coutens et al. (2014) and references therein.

^bThe unit of temperature (T) is the Kelvin.

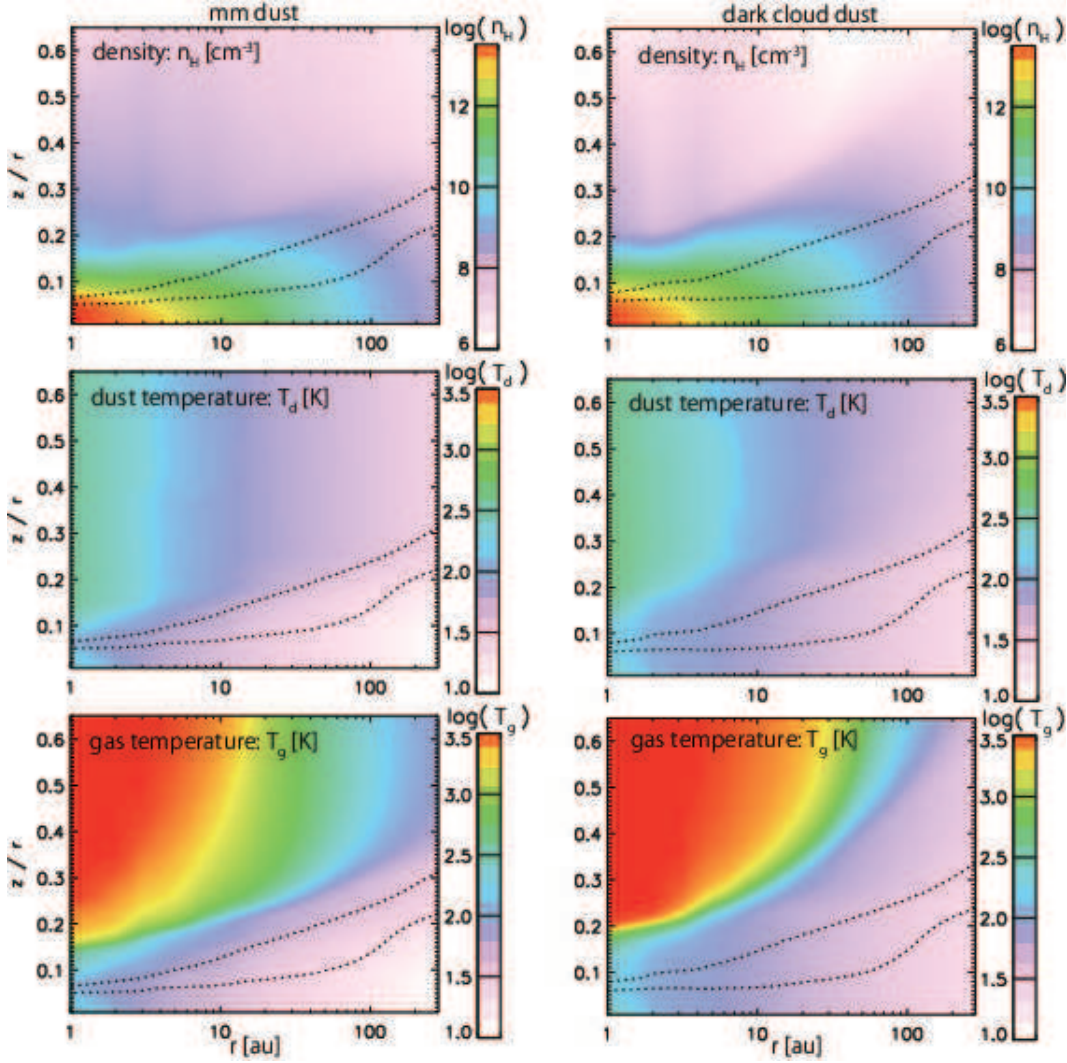


Fig. 1.— Distributions of gas density (top), dust temperature (middle), and gas temperature (bottom) in the disk model with mm-sized grains (left) and dark cloud dust (right). The upper dotted line depicts the positions where the X-ray ionization rate is equal to the cosmic-ray ionization rate ($5 \times 10^{-17} \text{ s}^{-1}$), while the X-ray ionization rate is $1 \times 10^{-18} \text{ s}^{-1}$ at the lower dotted line.

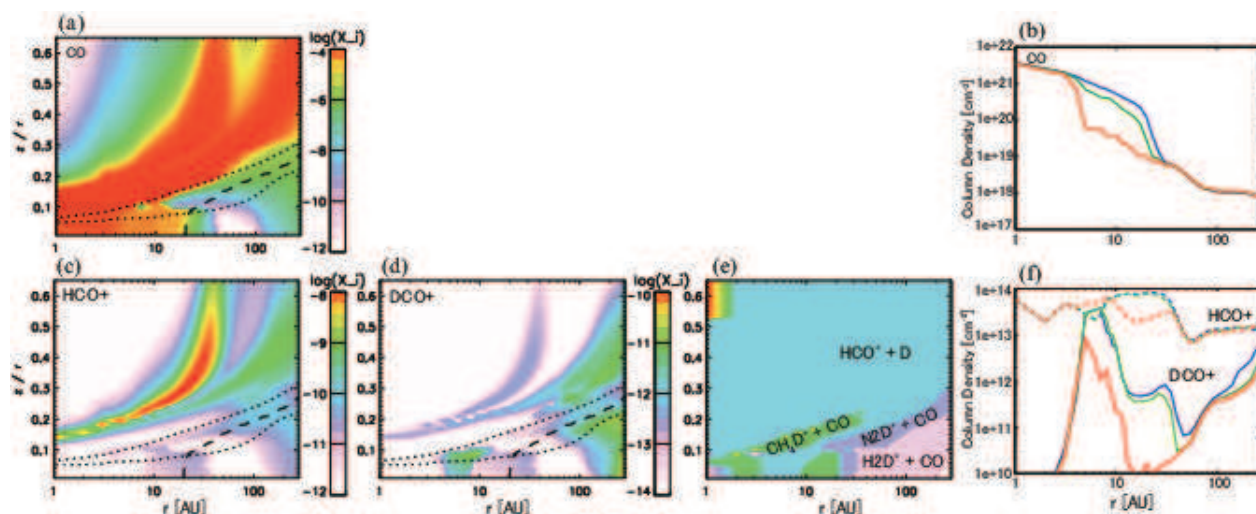


Fig. 2.— Panels (a), (c), and (d) depict distributions of CO, HCO⁺, and DCO⁺ in the gas phase in the disk model with mm-sized grains at 3×10^5 yr. The long dashed lines depict the CO snow surface, while the dotted lines are the same as in Figure 1. Panel (e) is color coded referring to the major formation pathways of DCO⁺ at each position in the disk. Panels (b) and (f) show the radial distribution of molecular column densities at 1×10^5 yr (blue), 3×10^5 yr (green), and 9.3×10^5 yr (red).

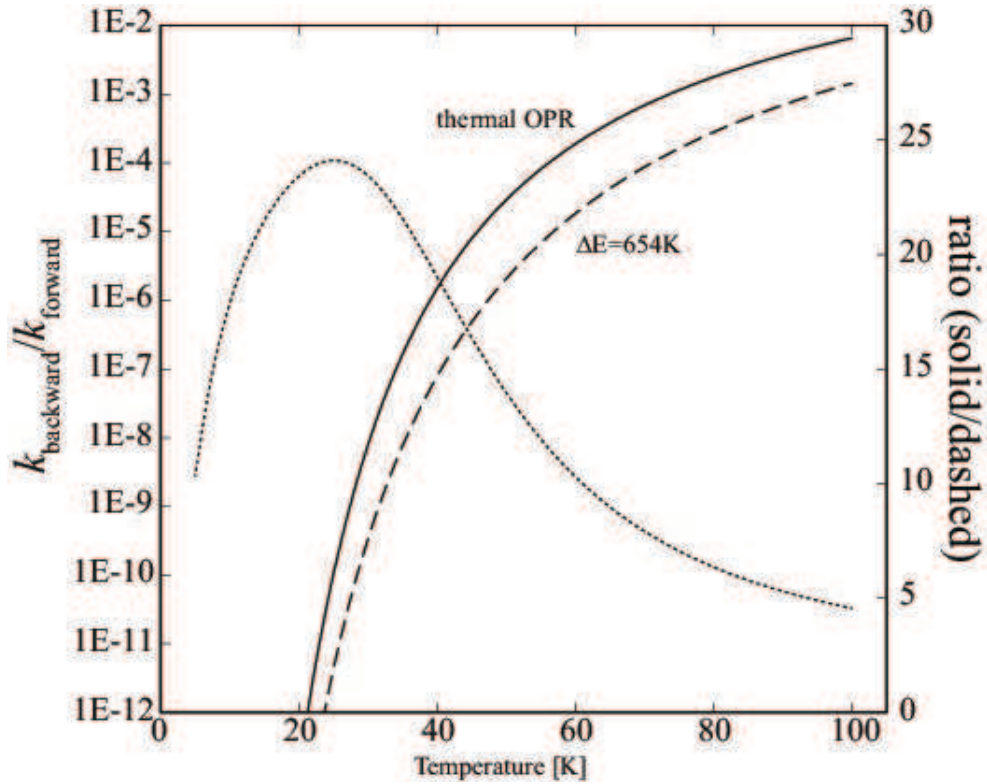


Fig. 3.— The ratio of backward to forward reaction rate coefficients of $\text{CH}_3^+ + \text{HD} \rightarrow \text{CH}_2\text{D}^+ + \text{H}_2$ (reaction 3) as a function of gas temperature given in Roueff et al. (2013). The solid line depicts the value with the thermal OPR of H_2 , while the dashed line depicts the value with a constant exothermicity of 654 K assuming all H_2 in the para form. The ratio of the former to the latter is shown by the dotted line.

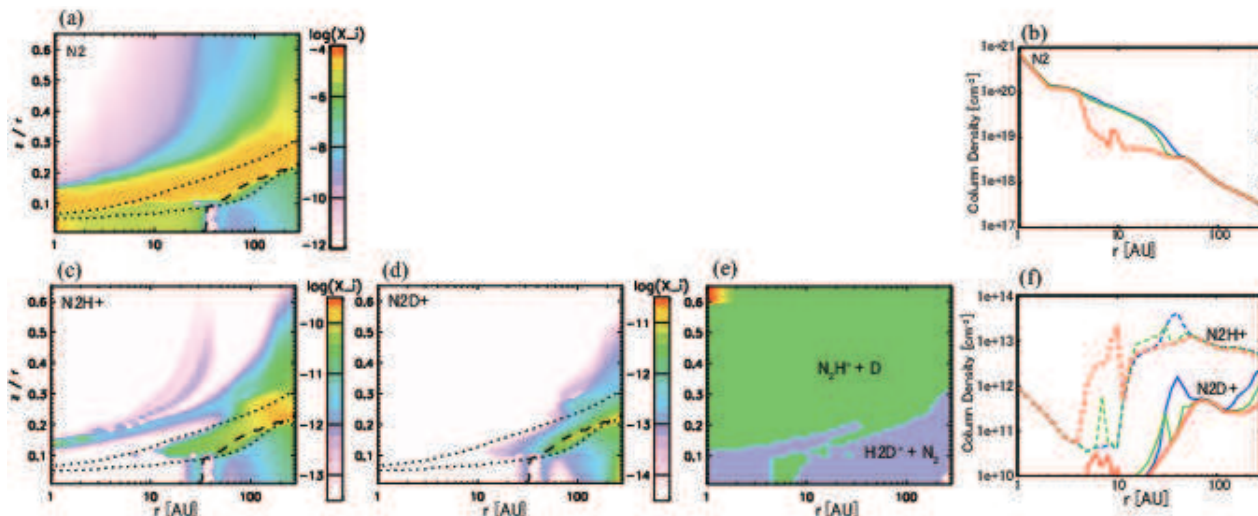


Fig. 4.— Distributions of molecular abundances (a, c, and d) and molecular column densities (b and f) as in Figure 2, but for N_2 , N_2H^+ , and N_2D^+ in the gas phase. The long dashed lines in panels (a), (c) and (d) depict the N_2 snow surface. Panel (e) is color coded referring to the major formation pathways of N_2D^+ at each position in the disk.

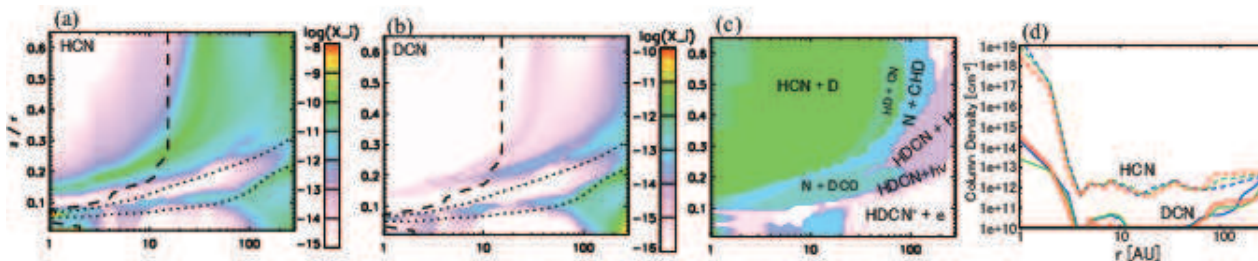


Fig. 5.— Distribution of molecular abundances (a-b) and molecular column densities (d) as in Figure 2, but for HCN , and DCN in the gas phase. The long dashed lines in panels (a) and (b) depict the HCN snow surface. Panel (c) is color coded referring to the major formation pathways of DCN at each position in the disk.

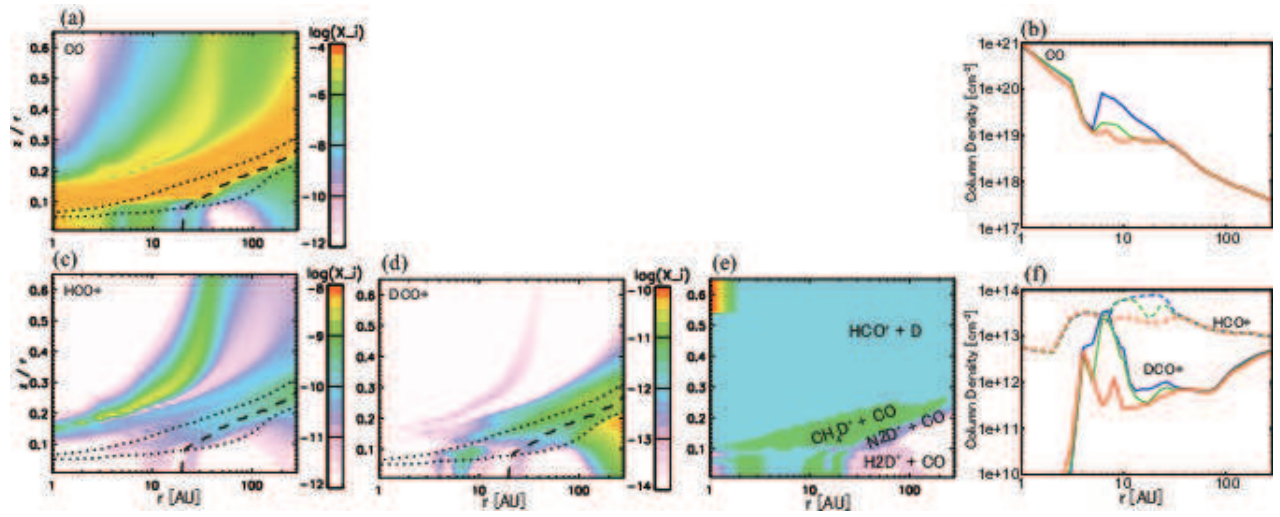


Fig. 6.— Same as Figure 2, but for the disk model with depletions of CO and H₂O. In panel (e), DCO⁺ is formed mainly via H₂D⁺ + CO in the pink region, while the reactions of multi-deuterated H₃⁺ with CO dominate in the white region.

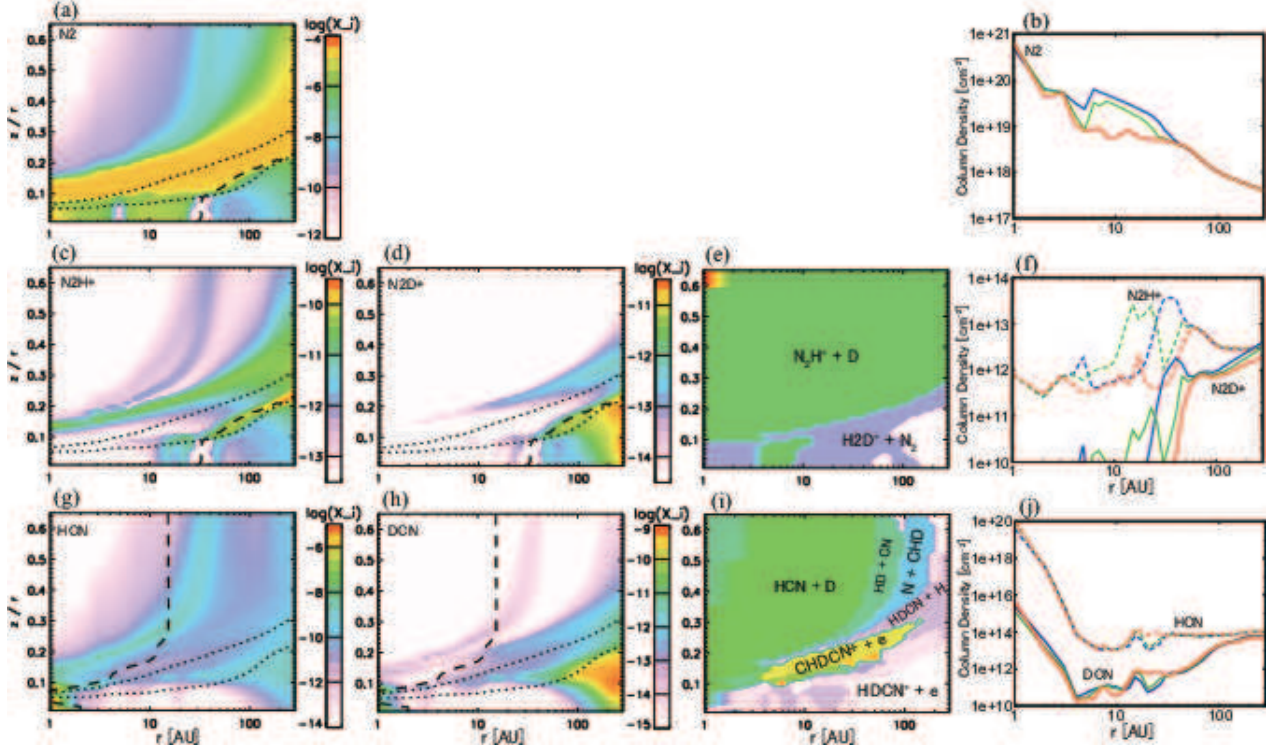


Fig. 7.— Distribution of molecular abundances (a, c, d, g and h), and molecular column densities (b, f, and j) as in Figure 2, but for N_2 , N_2H^+ , N_2D^+ , HCN and DCN in the gas phase in the disk model with depletions of CO and H_2O . The long dashed lines depict the snow surface of the mother molecule. Panels (e) and (i) are color coded referring to the major formation pathways of N_2D^+ and DCN, respectively, at each position in the disk. In panel (e), the reactions of multi-deuterated H_3^+ with N_2 dominate in the white region, while the reaction of $\text{H}_2\text{D}^+ + \text{N}_2$ dominates in the purple region.

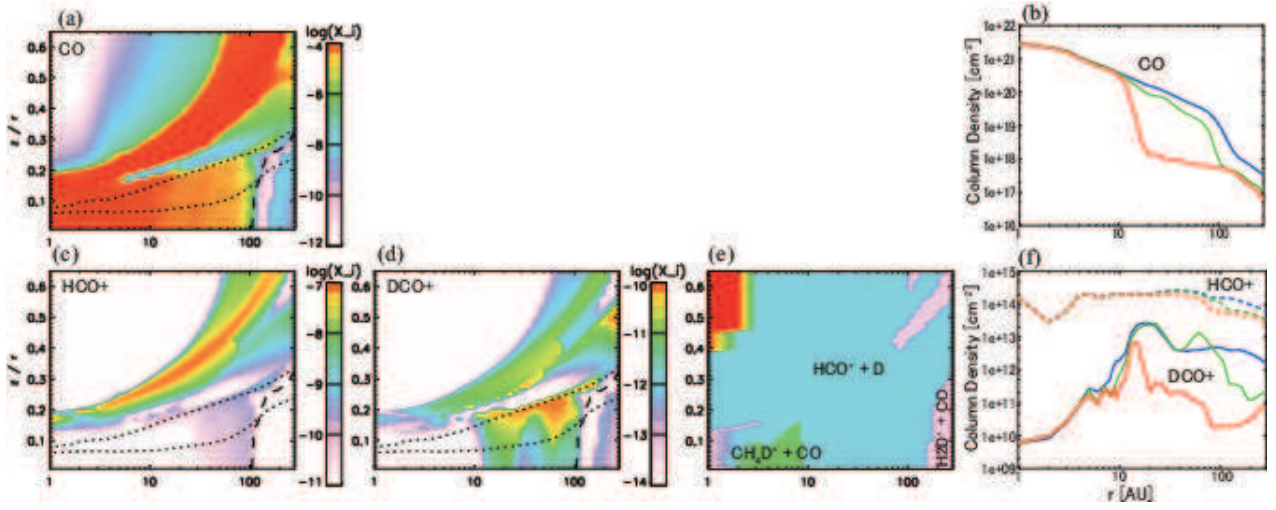


Fig. 8.— Same as Figure 2, but for the disk model with dark cloud dust.

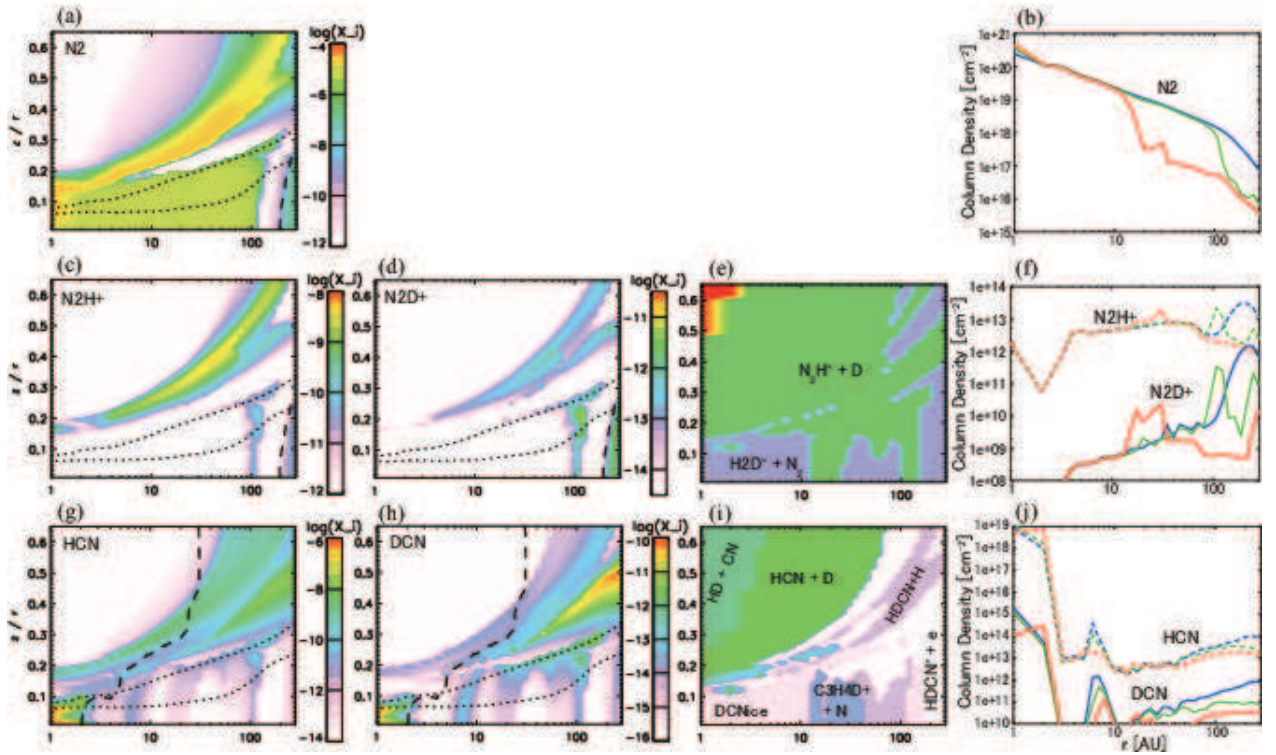


Fig. 9.— Same as Figure 7, but for the disk model with dark cloud dust.

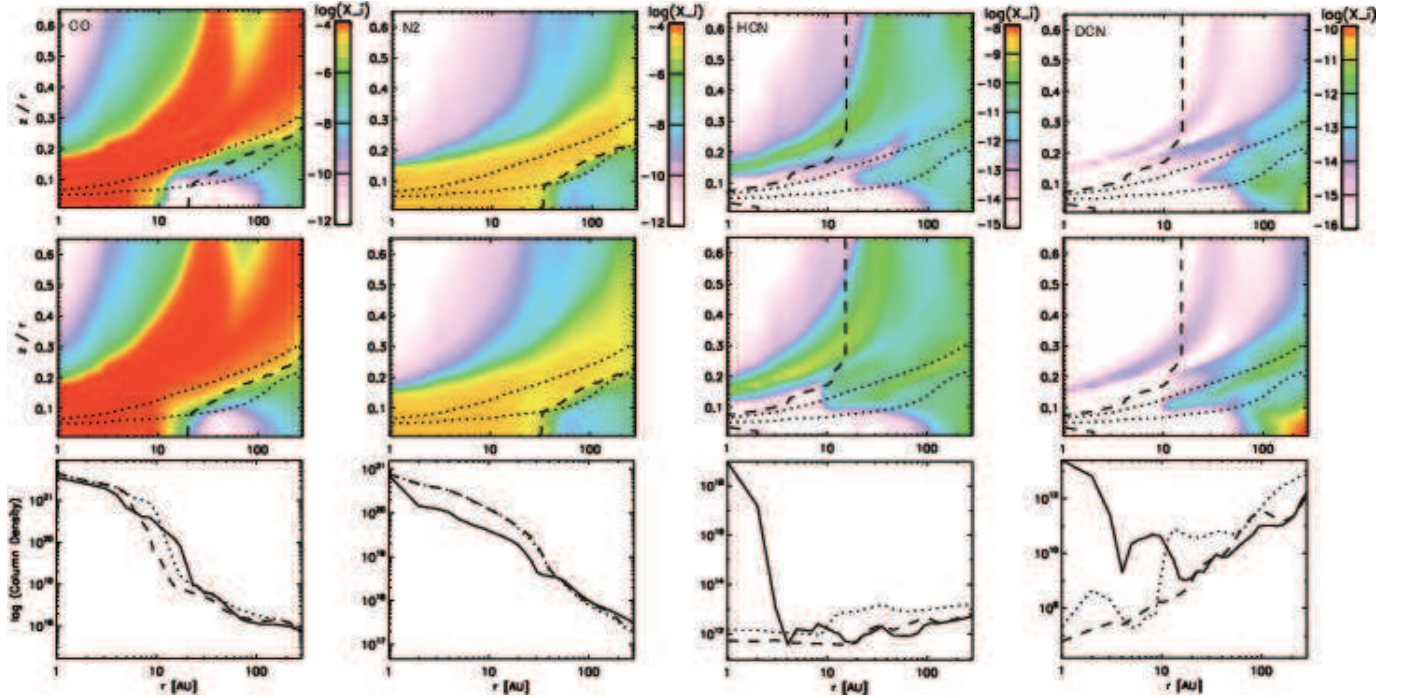


Fig. 10.— Distributions of gaseous CO, N₂, HCN and DCN in the mm-sized grain model with vertical mixing at $t = 3 \times 10^5$ yr. The diffusion coefficient is $\alpha = 10^{-3}$ in the top panels, and $\alpha = 10^{-2}$ in the middle panels. The bottom panels show the radial distribution of molecular column densities of models without diffusion (solid) and with a diffusion coefficient of 10^{-3} (dashed), and 10^{-2} (dotted) at $t = 3 \times 10^5$ yr.

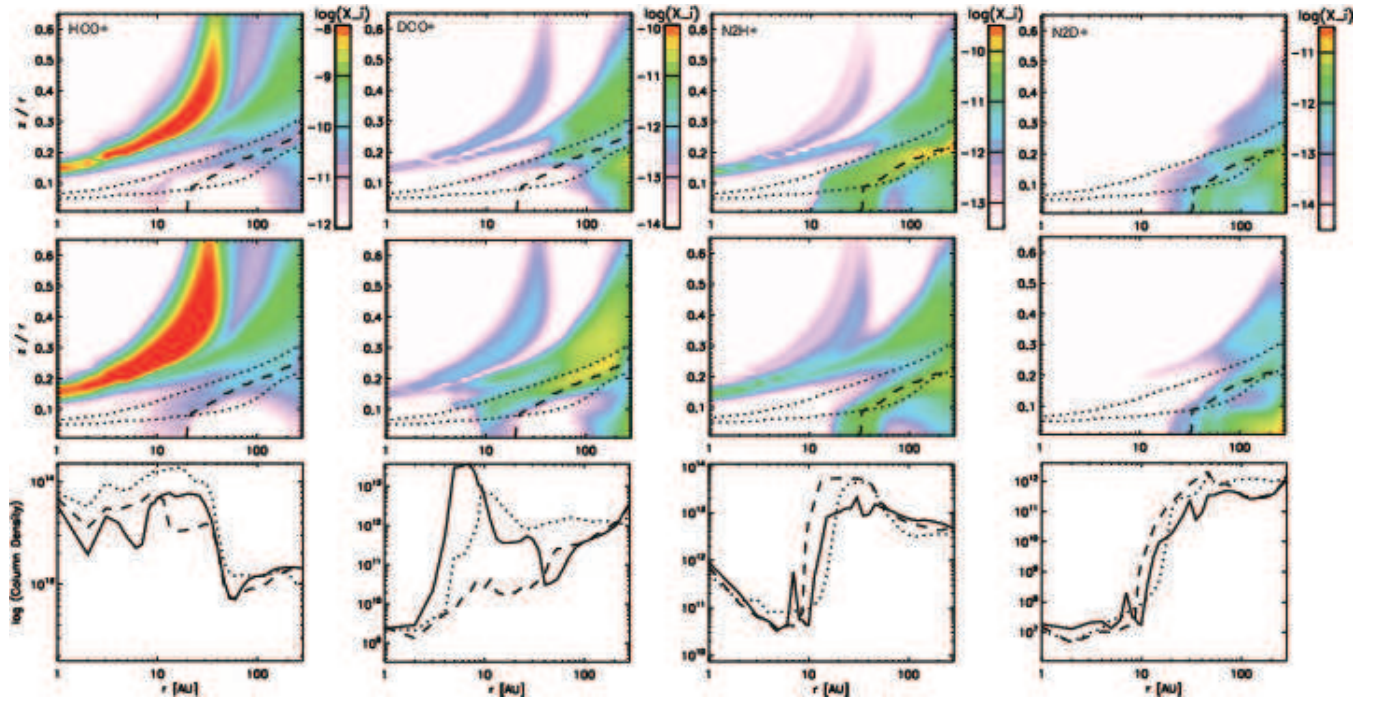


Fig. 11.— Same as Figure 10, but for ionic molecules.

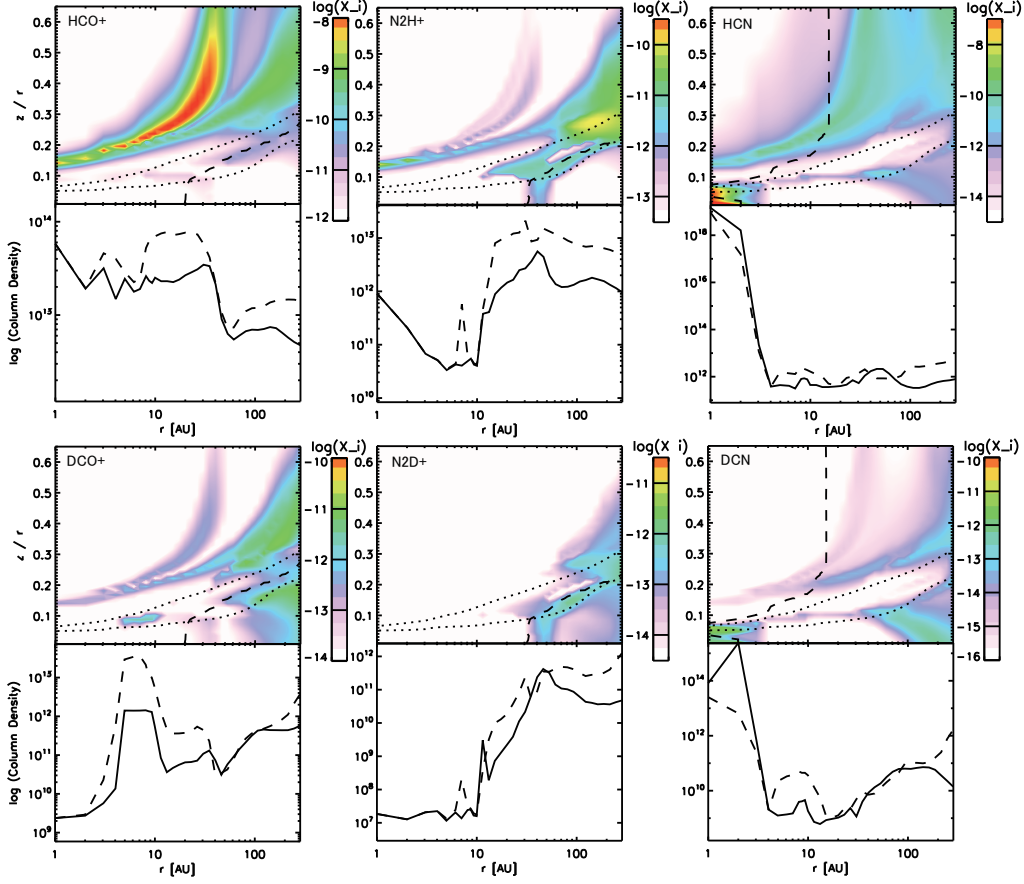


Fig. 12.— Distributions of abundances and column densities of HCO⁺, N₂H⁺, HCN and their deuterated isotopologs in the mm-sized grain model without cosmic-ray ionization at $t = 3 \times 10^5$ yr. The solid lines depict the molecular column density without cosmic-ray ionization, while the dashed lines depict the column density in our fiducial model.

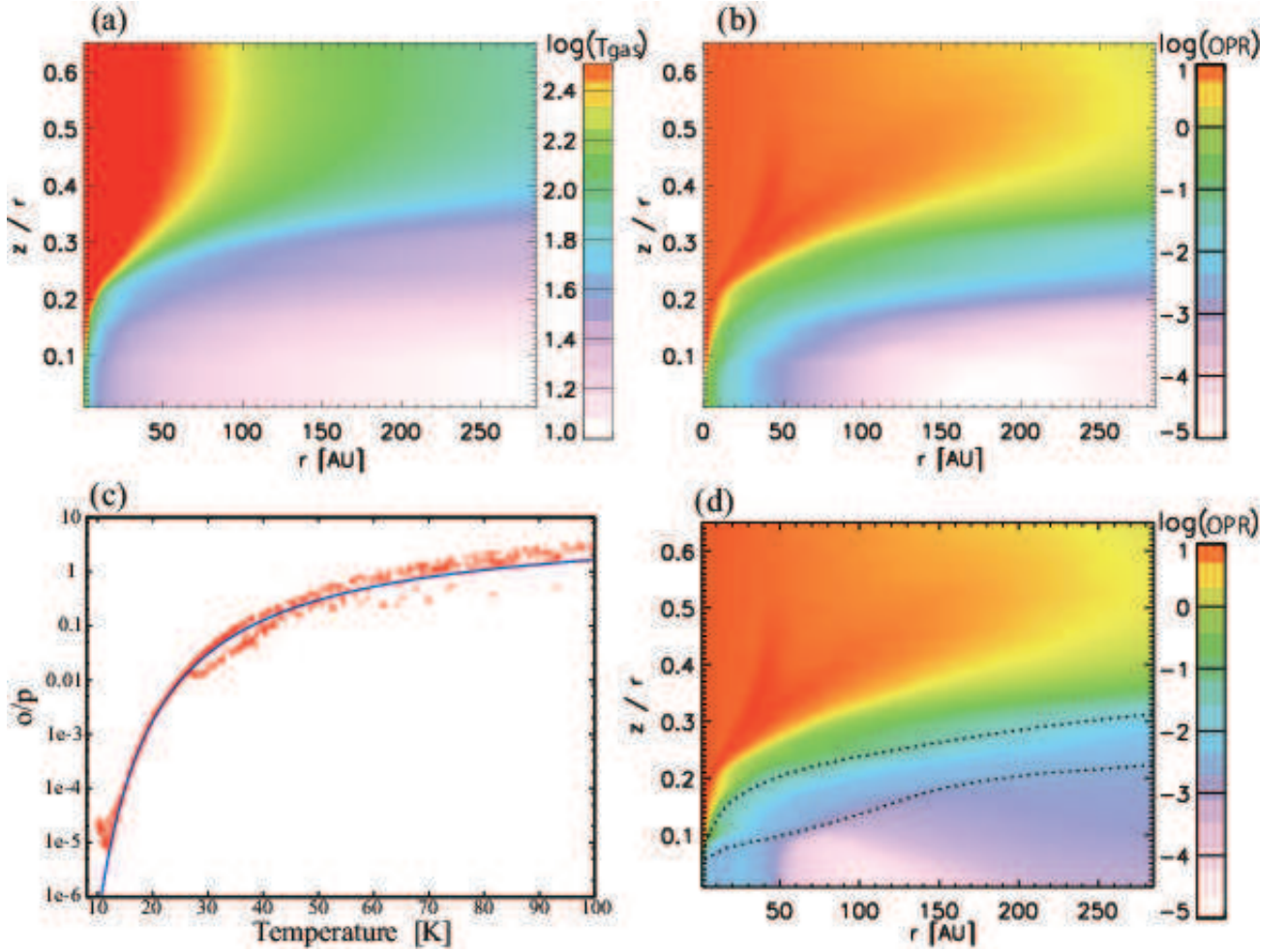


Fig. 13.— (a) Distribution of gas temperature in our fiducial disk model. (b) Distribution of H_2 OPR in our fiducial disk model. (c) H_2 OPR in our fiducial model (red crosses) and thermal equilibrium value (blue) as functions of temperature. (d) Same as (b), but for the model without cosmic-ray ionization. The upper and lower dotted lines depict the positions where the X-ray ionization rate is equal to $5 \times 10^{-17} \text{ s}^{-1}$ and $1 \times 10^{-18} \text{ s}^{-1}$, respectively.

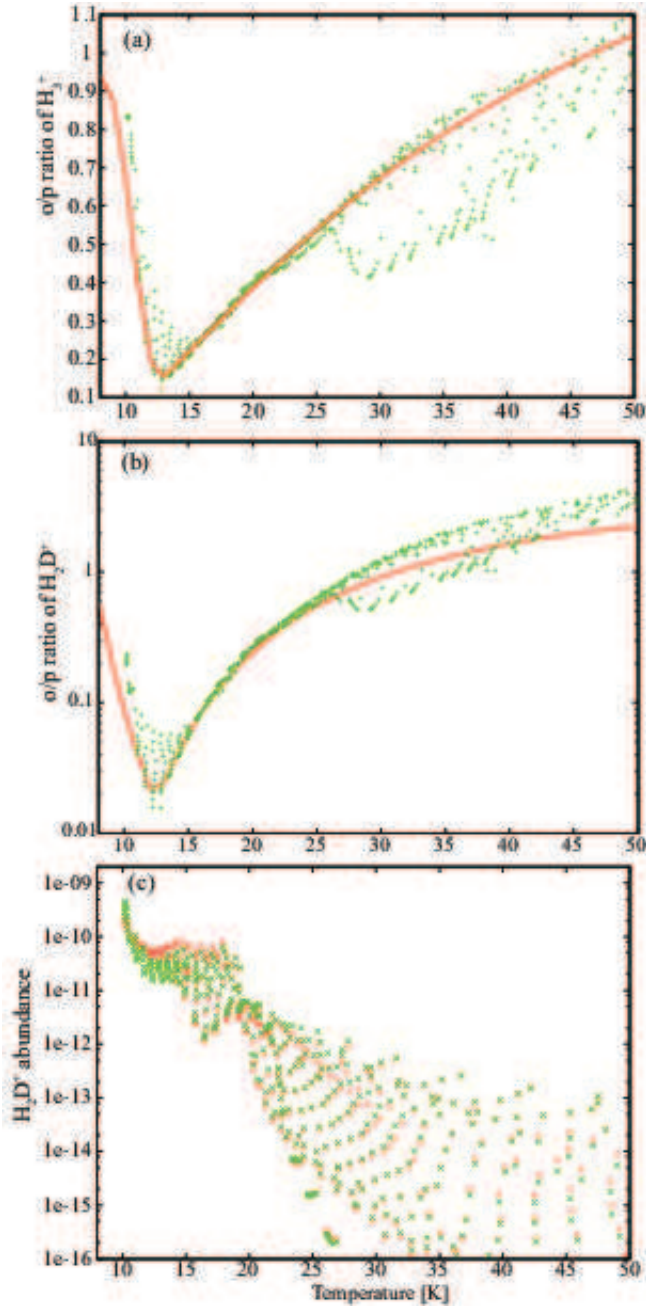


Fig. 14.— (a) OPR of H_3^+ in our fiducial model (green crosses) and thermal equilibrium value (red) as a function of temperature. (b) The o/p ratio of H_2D^+ in our fiducial model (green) and the analytical value (red). (c) H_2D^+ abundance in our fiducial model (green) and the value obtained by the analytical formula (red).

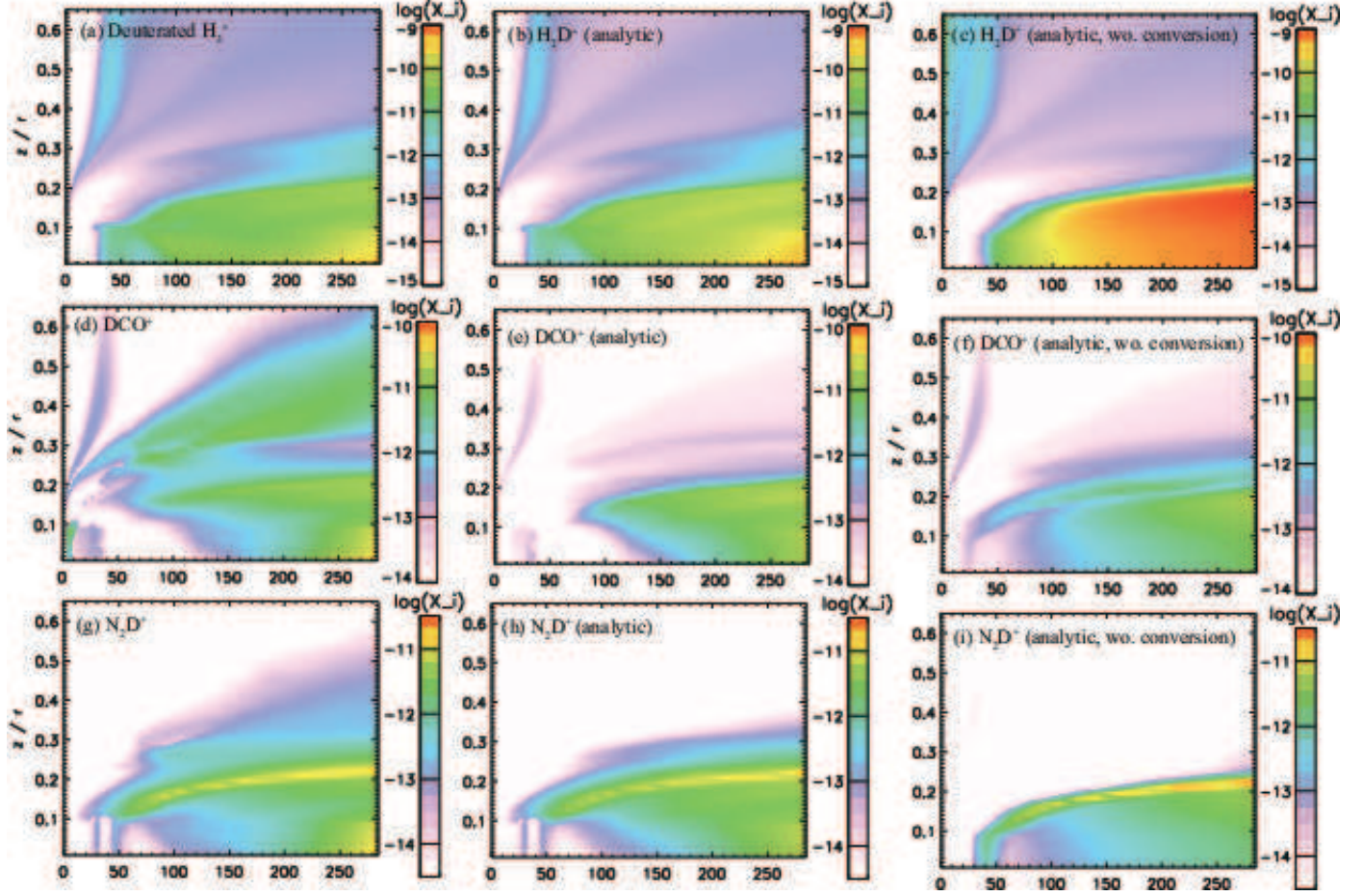


Fig. 15.— Panels (a), (d), and (g) show distributions of deuterated H_3^+ , DCO^+ and N_2D^+ in our fiducial model at $t = 3 \times 10^5$ yr. Panels (b), (e), and (h) show distributions of H_2D^+ , DCO^+ and N_2D^+ calculated by the analytical formulas using the abundances of HD, CO, N_2 , and electrons from the fiducial model. Panels (c), (f), and (i) show distributions of H_2D^+ , DCO^+ and N_2D^+ calculated by the analytical formulas with the abundances of HD, CO and N_2 given analytically.